bioRxiv preprint doi: https://doi.org/10.1101/2020.11.10.377333; this version posted November 11, 2020. The copyright holder for this preprint (which was not certified by peer review) is the author/funder, who has granted bioRxiv a license to display the preprint in perpetuity. It is made available under aCC-BY-NC-ND 4.0 International license.

Characterization and structural basis of a lethal mouse-adapted SARS-CoV-2

Shihui Sun[1†], Hongjing Gu[1†], Lei Cao[2†], Qi Chen[1†], Guan Yang[3†], Rui-Ting Li[1†], Hang Fan[1†], Qing Ye[1], Yong-Qiang Deng[1], Xiaopeng Song[3], Yini Qi[3], Min Li[1], Jun Lan[2], Rui Feng[2], Yan Guo[1], Si Qin[1], Lei Wang[2], Yi-Fei Zhang[1], Chao Zhou[1], Lingna Zhao[1], Yuehong Chen[1], Meng Shen[1], Yujun Cui[1], Xiao Yang[3], Xinquan Wang[4], Hui Wang[1*], Xiangxi Wang[2*], Cheng-Feng Qin[1*]

[1]State Key Laboratory of Pathogen and Biosecurity, Beijing Institute of Microbiology and Epidemiology, AMMS, Beijing 100071, China.

[2]CAS Key Laboratory of Infection and Immunity, National Laboratory of Macromolecules, Institute of Biophysics, Chinese Academy of Sciences, Beijing 100101, China.

[3] State Key Laboratory of Proteomics, Beijing Proteome Research Center, National Center for Protein Sciences (Beijing), Beijing Institute of Lifeomics Beijing 102206, China.

[4]The Ministry of Education Key Laboratory of Protein Science, Beijing Advanced Innovation Center for Structural Biology, Beijing Frontier Research Center for Biological Structure, Collaborative Innovation Center for Biotherapy, School of Life Sciences, Tsinghua University, 100084 Beijing, China

*Corresponding to: Cheng-Feng Qin (qincf@bmi.ac.cn), Xiangxi Wang (xiangxi@ibp.ac.cn), or Hui Wang (geno0109@vip.sina.com)

†These authors contributed equally.

bioRxiv preprint doi: https://doi.org/10.1101/2020.11.10.377333; this version posted November 11, 2020. The copyright holder for this preprint (which was not certified by peer review) is the author/funder, who has granted bioRxiv a license to display the preprint in perpetuity. It is made available under aCC-BY-NC-ND 4.0 International license.

Abstract

The ongoing SARS-CoV-2 pandemic has brought an urgent need for animal models to study the pathogenicity of the virus. Herein, we generated and characterized a novel mouse-adapted SARS-CoV-2 strain named MASCp36 that causes acute respiratory symptoms and mortality in standard laboratory mice. Particularly, this model exhibits age and gender related skewed distribution of mortality akin to severe COVID-19, and the 50% lethal dose (LD50) of MASCp36 was ~100 PFU in aged, male BALB/c mice. Deep sequencing identified three amino acid mutations, N501Y, Q493H, and K417N, subsequently emerged at the receptor binding domain (RBD) of MASCp36, which significantly enhanced the binding affinity to its endogenous receptor, mouse ACE2 (mACE2). Cryo-electron microscopy (cryo-EM) analysis of mACE2 in complex with the RBD of MASCp36 at 3.7-angstrom resolution elucidates molecular basis for the receptor-binding switch driven by amino acid substitutions. Our study not only provides a robust platform for studying the pathogenesis of severe COVID-19 and rapid evaluation of coutermeasures against SARS-CoV-2, but also unveils the molecular mechanism for the rapid adaption and evolution of SARS-CoV-2 in mice.

One sentence summary

A mouse adapted SARS-CoV-2 strain that harbored three amino acid substitutions in the RBD of S protein showed 100% mortality in aged, male BALB/c mice.

bioRxiv preprint doi: https://doi.org/10.1101/2020.11.10.377333; this version posted November 11, 2020. The copyright holder for this preprint (which was not certified by peer review) is the author/funder, who has granted bioRxiv a license to display the preprint in perpetuity. It is made available under aCC-BY-NC-ND 4.0 International license.

Introduction

Coronavirus disease 2019 (COVID-19) caused by severe acute respiratory syndrome coronavirus 2 (SARS-CoV-2), has resulted in a public health crisis (*1*). The symptoms of COVID-19 are similar to those of SARS-CoV and MERS-CoV infections, ranging from fever, fatigue, dry cough and dyspnea, and mild pneumonia to acute lung injury (ALI) and the acute respiratory distress syndrome (ARDS) in severe cases. In fatal cases, multi-organ failures accompanied by a dysregulated immune response have been observed (*2-4*). Numerous studies have highlighted age and gender related discrepancies in the distribution of COVID-19 cases where the elderly and men tend to have a higher case-fatality ratio when compared to the young and females, suggesting that aged man are more likely to succumb to COVID-19 (*5*, *6*).

Similar to SARS-CoV, SARS-CoV-2 belongs to the *Betacoronavirus* genus of the *Coronaviridae* family, and is an enveloped, single stranded positive-sense RNA virus. Human angiotensin-converting enzyme 2 (ACE2), has been demonstrated as the functional receptor for SARS-CoV-2 (*7*, *8*). SARS-CoV-2 cannot infect wild-type laboratory mice due to inefficient interactions between its S protein and the ACE2 receptor of mouse (mACE2). (*9*). So, several hACE2 expressing mouse models such as hACE2 transgenic mice (*10*), AAV-hACE2 transduced mice (*11*) and Ad5-hACE2 transduced mice (*12*) have been developed. Furthermore, mouse adapted strains of SARS-CoV-2 have also been developed *via* either *in vivo* passaging or reverse genetics (*13-15*). However, all these models cause only mild to moderate lung damage in mice. A small animal model capable of recapitulating the severe respiratory symptoms and high case fatality ratio of COVID-19 remains to be established.

In this study, we have developed and characterized a new lethal strain of SARS-CoV-2 named MASCp36 by using the *in vivo* passaging method. Previously, we reported the development of MASCp6, a mouse-adapted SARS-CoV-2 strain using a similar strategy (*16*). Remarkably, intranasal injection of MASCp36 caused 100% fatality in aged BALB/c mice. Prior to death, all infected animals developed severe malfunctions of the respiratory system, including acute respiratory distress syndrome (ARDS) characterized by breathlessness and multi-organ damage. Deep sequencing identified a panel of amino acid substitutions distributed across the genome of MASCp36. Notably, three of these mutations are located in the RBD of S protein.

bioRxiv preprint doi: https://doi.org/10.1101/2020.11.10.377333; this version posted November 11, 2020. The copyright holder for this preprint (which was not certified by peer review) is the author/funder, who has granted bioRxiv a license to display the preprint in perpetuity. It is made available under aCC-BY-NC-ND 4.0 International license.

Binding affinities between mACE2 and the RBD from the mouse-adapted strains at different passages correlate closely with the emergence of progressively enhanced virulence phenotype in mice, reflecting an adapted evolution of SARS-CoV-2. Analysis of the structures of the mACE2 in complex with the RBDs of MASCp25 and MASCp36 identified residues of the RBD that underpin the various binding affinities and infectivity of serially mouse-adapted strains, shedding light on the molecular basis for cross-transmission of SARS-CoV-2. In addition, the utility of lethal MASCp36 infected mouse model in evaluation of therapeutics against COVID-19 was studied by using a potent human neutralizing antibody. Thus, the mouse-adapted MASCp36 opens up a unique opportunity for developing a lethal mouse model for studying the pathogenesis of severe cases of COVID-19, or evaluating the effectiveness of vaccines and therapeutics against COVID-19.

Results

Generation of a lethal mouse-adapted strain of SARS-CoV-2

In our previous study, we generated a mouse-adapted strain of SARS-CoV-2 (MASCp6) by 6 serial passages of a SARS-CoV-2 in the lung of aged BALB/c mice, which caused moderate lung damage and no fatality in mice. Herein, we further serially passaged for additional 30 times to generate a more virulent SARS-CoV-2, and the resulting virus at passage 36 (named as MASCp36) was used for stock preparation and titration.

To characterize the pathogenicity of MASCp36, groups of BALB/c were subjected to intranasal injection of varying doses of MASCp36. Strikingly, survival curve analysis showed that high doses of MASCp36 caused almost 100% mortality within ten days in all aged mice, while young mice were resistant to MASCp36 challenge and no animals developed disease and died in this group (Fig. 1A-D). Aged mice challenged with high dose of MASCp36 developed typical respiratory symptoms and exhibited features like ruffled fur, hunched back, and reduced activity. Of particular note, tachypnea was common in all moribund animals (supplemental video). For the aged mice, male animals were more susceptible to MASCp36 in comparison to female ones, and the LD50 was calculated to 58 PFU and 690 PFU, respectively (Fig. 1A, B). Additionally, this unique gender-dependent mortality was also recorded in aged C57BL/6 mice challenged with MASCp36 (fig. S1) where 80% of the males challenged with the virus died from respiratory symptoms. Thus, serial passaging of MASCp6 generated a more

bioRxiv preprint doi: https://doi.org/10.1101/2020.11.10.377333; this version posted November 11, 2020. The copyright holder for this preprint (which was not certified by peer review) is the author/funder, who has granted bioRxiv a license to display the preprint in perpetuity. It is made available under aCC-BY-NC-ND 4.0 International license.

virulent MASCp36, which was sufficient to cause 100% mortality in aged BALB/c mice at low dose (~1200 PFU).

We further characterized the *in vivo* replication dynamics of MASCp6 in both young and aged mice, and the results from qRT-PCR showed that high levels of SARS-CoV-2 subgenomic RNAs were persistent in the lung and tracheas till 4 day post infection (dpi) in aged mice (Fig. 1E). Marginal viral RNAs were also detected in the intestine, heart, liver, spleen, brain, and kidney. The young mice had a similar tissue distribution as the aged ones upon MASCp36 challenge, and lung and tracheas represented the major tissues supporting viral replication (Fig. 1F). Multiplex immuno staining showed that MASCp36 predominantly targeted the airway CC10+ club cells and SPC+ AT2 cells, while FOXJ1+ ciliated cells and PDPN+ alveolar type 1 (AT1) cells detected few positive signals (Fig. 1G). More SARS-CoV-2-infected cells were detected in the lung from aged mice than those from young animals at 1 dpi (Fig. 1H), which was in agreement to the high ratio of SPC+ AT2 cells that co-express ACE2 in aged mice (fig. S2). Consequently, a striking loss of SPC+ AT2 cells with apoptosis were observed in the lung from aged mice (fig. S3). Collectively, aged male mice that developed severe respiratory symptoms and 100% fatality serve as the most suitable animal host for MASCp36 and were chosen for subsequent analysis.

MASCp36 causes multiple organ damage akin to COVID-19 in mice

To further characterize the pathogical outcome in MASCp36 infected aged male mice, the lung as well as other organs were collected at 4 dpi and subjected to histopathological and immunostaining analysis. When observed by the naked eye, lung tissue samples from MASCp36 infected animals showed visible lung injury characterized with biolateral cardinal red appearance. Furthermore, a lot of sticky secretion was seen at the lung surfaces when compared with the control animals (Fig. 2A). According to the metrics of acute lung injury (ALI) laid out by the American Thoracic Society (ATS), MASCp36 infection induced necrotising pneumonia and extensive diffuse alveolar damages (DAD) and even ARDS on day 4 (*17*). The microscopic observation showed large quantities of desquamative epithelial cells in bronchiole tubes (yellow arrow) and a large area of necrotic alveoli epithelial cells, fused alveoli walls with inflammatory cells infiltration especially neutrophils in alveolar septae or alveolar airspace, serious edema around vessels (cyan arrow) and

bioRxiv preprint doi: https://doi.org/10.1101/2020.11.10.377333; this version posted November 11, 2020. The copyright holder for this preprint (which was not certified by peer review) is the author/funder, who has granted bioRxiv a license to display the preprint in perpetuity. It is made available under aCC-BY-NC-ND 4.0 International license.

scattered hemorrhage (blue arrow) (Fig. 2A). In addition, foamy cells, polykaryocytes, fibrin cluster deposition, and hyaline membrane formation were common in the MASCp36 infected animals (Fig. 2B), indicative of acute respiratory distress syndrome (ARDS), which is well characterized in severe COVID-19 patients (*4*). Interestingly, typical viral inclusion bodies were also observed occasionally in lungs of infected mice (Fig. 2B). Comparatively, lung damage in young mice infected with MASCp36 were much milder than those of the aged mice; less visual lung damage were seen in gross necropsy, and only thickened alveolar septa and activated inflammatory cell infiltration were observed in young mice at 4 dpi.(fig.S4).

Apart from the lung damage, spleen damage characterized by atrophic splenic corpuscle, splenic cells necrosis and hemorrhage in red pulp were obvious in aged mice at day 4 pi (Fig. 2C). Results of the multiplex immunofluorescence studies showed a striking loss of germinal centers in the spleen of infected aged mice as suggested by the reduction in $CD19^+$ B and $CD3^+$ T cell counts as well as diminished $ICOS^+$ follicular helper T cells in the stained samples (Fig. 2E) which indicated damage to host immune responses as a result of the viral infection and faithfully mimics the observations recorded in severe COVID-19 patients (*18*). In addition, renal tubular damage with casts in renal tubules, as well as breakdown of $CD31^+$ glomerular capillary epithelium and $PDPN^+$ basement membrane were observed in kidney (fig. S5). The splenic lesion and kidney damage were also reported in cases with postmortem examinations of deceased COVID-19 patients (*19, 20*). These pathological damages caused by MASCp36 in mice recapitulated most spectrums of seriously ill COVID-19 patients caused by SARS-CoV-2 infection.

MASCp36 induces robust inflammatory response in mice

To further characterize the transcriptional response to infection of MASCp36 in male, aged BALB/c mice, RNA-Seq analysis were performed using lung homogenates collected at 4 dpi. Volcano plots showed a total of 1770 up-regulated genes and 1313 down-regulated genes in response to MASCp36 infection. Within these, cytokines IL-6 and CCL-2 were among the top 20 up-regulated genes (fig. S6A). Gene enrichment analyses showed that MASCp36 infection induced strong transcription of genes related to antiviral response, inflammatory, cell death and cytokine production (fig. S6B). Of particular note, a large amount of cytokine and chemokines transcription were up

bioRxiv preprint doi: https://doi.org/10.1101/2020.11.10.377333; this version posted November 11, 2020. The copyright holder for this preprint (which was not certified by peer review) is the author/funder, who has granted bioRxiv a license to display the preprint in perpetuity. It is made available under aCC-BY-NC-ND 4.0 International license.

regulated in response to MASCp36 (fig. S6D). Meanwhile, Luminex analysis also detected obvious elevated cytokine and chemokine production, including IL-6, IFN-γ, CCL20 and CCL7, in the lung homogenates from MASCp36 infected mice (fig. S6D). Additionally, immunostaining of lung sections showed a significant infiltration of $CD68^+$ macrophages and Ly-$6G^+$ neutrophils in MASCp36 infected mice (fig. S7). Interestingly, more $CD68^+$ macrophages and Ly-$6G^+$ neutrophils were detected in young mice than that in aged mice 1 dpi, and reversed on 4 dpi, which indicated rapid and short-lived immune response to limite viral replication in young mice.

H014 confers full protection in lethal MASCp36 model

To test the utility of MASCp36 infected mouse model for evaluation of antiviral candidates, H014, a known human monoclonal antibody targeting the RBD of SARS-CoV-2 (*21*), was examined for its ability to confer benefit during the infection. Administration of a single dose of H014 (50 mg/kg) resulted in 100% survival and complete clearance of virus from the lungs of infected mice. By contrast, all animals that received a control isotype antibody treatment showed high levels of viral replication in lungs and eventually died with respiratory diseases within 5 days (Fig. 3A and 3B). Multiplex immunofluorescence staining confirmed H014 treatment completely protected animals from viral infection and replication by preventing AT2 loss and neutrophil infiltration caused as a result of MASCp36 infection (Fig. 3C). H&E staining also showed that H014-treatment significantly prevented the MASCp36-induced lung damage characterized by a large area of fused alveoli walls, desquamative epithelial cells, severe edema and scattered hemorrhage (Fig.3D). These results highlight the potential of MASCp36-based models in evaluating the antiviral activity of therapeutics in treating COVID-19.

Adaptive mutations responsible for the enhanced virulence of MASCp36

To deduce the genetic basis for the lethal phenotype of MASCp36, deep sequencing was performed to identify the mutations emerged during the *in vivo* passaging history. Sequence comparisons of WT and serially mouse-adapted strains (MASCp6, MASCp25 and MASCp36) revealed a process of gradual accumulation of amino acid substitutions during the course of viral adapted evolution (fig S8). A total of 12 amino acid substitutions were identified throughout the whole genome. Interestingly, single (N501Y), double (Q493H, N501Y) and triple (K417N, Q493H, N501Y) mutations in

bioRxiv preprint doi: https://doi.org/10.1101/2020.11.10.377333; this version posted November 11, 2020. The copyright holder for this preprint (which was not certified by peer review) is the author/funder, who has granted bioRxiv a license to display the preprint in perpetuity. It is made available under aCC-BY-NC-ND 4.0 International license.

the RBD were identified in MASCp6, MASCp25 and MASCp36, respectively (Fig. 4A and fig. S8B). To clarify the potential role of these mutations, the RBD of these different adaptive strains were expressed to assay their binding affinities to mACE2 (fig. S9). As expected, the WT RBD presented no detectable binding, but RBDs from mouse-adapted strains (RBD_{MASCp6}, $RBD_{MASCp25}$ and $RBD_{MASCp36}$) gain gradually enhanced binding abilities to mACE2 with affinities ranging from ~500 μM to 2 μM (Fig. 4B). The increased affinity between mACE2 and the RBD of mouse-adapted strains probably contribute to the enhanced virulence in mice.

Structural basis for the enhanced virulence of MASCp36

To further elucidate the molecular basis for the gradual change in specificity of MASCp36, structural investigations of the mACE2 in complex with $RBD_{MASCp25}$ or $RBD_{MASCp36}$ were carried out. Two non-competing Fab fragments that recognize the RBD beyond the mACE2 binding sites were used to increase the molecular weight of this complex for pursuing an atomic resolution by cryo-EM reconstruction (fig. S9-S12). Interestingly, cryo-EM characterization of the mACE2 in complex with $RBD_{MASCp25}$ revealed that the complex adopts three distinct conformational states, corresponding to tight binding (state 1), loose binding (state 2) and no binding modes (state 3) (fig. S13), indicative of a quick association and quick dissociation interaction manner between the mACE2 and $RBD_{MASCp25}$. However, only the tight binding conformation was observed in the mACE2-$RBD_{MASCp36}$ complex structure, reflecting a more stable/mature binding mode for the $RBD_{MASCp36}$ to mACE2, akin to that of the RBD_{WT} and hACE2. We determined asymmetric cryo-EM reconstructions of the mACE2-$RBD_{MASCp36}$ complex at 3.7 Å and three states of the mACE2-$RBD_{MASCp25}$ complex at 4.4 to 8.2 Å (figs. S11-S12 and table S1). The map quality around the mACE2-$RBD_{MASCp36}$ interface was of sufficient quality for a reliable analysis of the interactions (Fig. 4C and fig. S9).

The overall structure of the mACE2-$RBD_{MASCp36}$ complex resembles that of the RBD_{WT}-hACE2 complex with a root mean square deviation of 1.0 Å (Fig. 4C). The $RBD_{MASCp36}$ recognizes the helices (α1 and α2) located at the apical region of the mACE2 *via* its receptor binding motif (RBM) (Fig 4C-4E). The interaction area on the mACE2 could be primarily divided into three patches (PI, PII and PIII), involving extensive hydrophilic and hydrophobic interactions with three regions separately

bioRxiv preprint doi: https://doi.org/10.1101/2020.11.10.377333; this version posted November 11, 2020. The copyright holder for this preprint (which was not certified by peer review) is the author/funder, who has granted bioRxiv a license to display the preprint in perpetuity. It is made available under aCC-BY-NC-ND 4.0 International license.

clustered by three adaptation-mediated mutated residues (K417N, corresponding to Clus1; Q493H, corresponding to Clus2; and N501Y, corresponding Clus3) in the RBM (Fig 4C-4E). Coincidentally, a number of amino acid substitutions, such as Q493K, Q498Y and P499T, in the RBM identified in other reported mouse-adapted SARS-CoV-2 isolates(*15, 22, 23*) were included either in the Clus2 or Clus3, underlining the putative determinants for cross-transmission (Fig 4F-4G). An extra Clus1 is further accumulated in the MASCp36 to gain utmost binding activity and infection efficacy (Fig 4F-4G). The extensive hydrophobic interactions in Clus3 constructed by Y501 (or Y498 or H498 in other mouse-adapted SARS-CoV-2 isolates), Y505 in the $RBD_{MASCp36}$ and Y41, H353 in the mACE2, hydrogen bonds in Clus2 formed H493 (K493 in other mouse-adapted strain) in the $RBD_{MASCp36}$ and N31, E35 in the mACE2 and hydrophilic contacts constituted by N417 in the $RBD_{MASCp36}$ and N30, Q34 in the mACE2 contribute to the tight binding of the MASCp36 to mACE2. Contrarily, structural superimposition of the RBD_{WT} over the mACE2-$RBD_{MASCp36}$ complex reveals the loss of these interactions, leading to the inability of the RBD_{WT} to bind mACE2 (Fig 4G). These analysis pinpoints key structure-infectivity correlates, unveiling the molecular basis for adaptation-mediated evolution and cross-transmission of SARS-CoV-2.

Discussion

Clinically, the severe COVID-19 disease onset might result in death due to massive alveolar damage and progressive respiratory failure (*24-26*). Distinct from all currently reported animal models which mimic the mild to moderate clinical symptoms of COVID-19, the MASCp36 infected mouse model could manifest many of the severe clinical syndromes associated with COVID-19 disease such as pulmonary oedema, fibrin plugs in alveolar, hyaline membrane, and scattered hemorrhage (*25, 27*). The complicated immunopathological phenomena observed in severe COVID-19 patients, such as massive macrophages and neutrophils infiltration, and excessively increased proinflammatory cytokines such as IL-6, were also observed in this MASCp36 infected mouse model. More importantly, the MASCp36 infection could lead to death in laboratory standard BALB/c and C57BL/6 mice with clearly defined genetic background, indicating its promising applications.

Aged mice infected with MASCp36 mimic the typical symptoms of severe COVID-19, including diffused alveolar damage (DAD) in lungs. Unlike serious pulmonary

bioRxiv preprint doi: https://doi.org/10.1101/2020.11.10.377333; this version posted November 11, 2020. The copyright holder for this preprint (which was not certified by peer review) is the author/funder, who has granted bioRxiv a license to display the preprint in perpetuity. It is made available under aCC-BY-NC-ND 4.0 International license.

fibrosis and vasodilation observed in SARS infections, SARS-CoV-2 causes more sticky secretions, which indicate severe damage of vasculature. In this model, thick fluid in pericardial cavity, hemorrhage and severe edema with less lymphocyte-cuff were observed in lung tissue, greatly resembling clinical manifestations of COVID-19. As the functional receptor of SARS-CoV and SARS-CoV-2, ACE2, is highly expressed on vascular endothelial cells and smooth muscle cells in multiple organs, which probably leads to the observed viral tropism contributing to cellular injury.

In this model, closely correlated with the higher ratio of ACE2-positive cells in type II pneumocytes in aged mice when compared to those in young mice, massive injury of (AT2 cells) type II pneumocytes was observed in aged mice. Therefore, age-related ACE2 expression pattern in lungs might contribute to the severe phenotype observed in aged mice. Although SARS-CoV-2 viral antigen has been detected in kidney of post-mortem specimens (*28*), no viral antigen or viral RNA were detected in our model. So in this MASCp36 infected mouse model, the kidney injury may arise due to secondary endothelial injury leading to proteinuria. In addition, although SARS-CoV-2 has also been implicated to have neurotropic potential in COVID-19 (*29*), we did not find typical characteristics of viral encephalitis in this model. Importantly, the imbalanced immune response with high-levels of proinflammatory cytokines, increased neutrophils and decreased lymphocytes, which were in line with SARS and MERS infections (*30*), playing a major role in the pathogenesis of COVID-19 (*31*), were also observed in this model.

The skewed age distribution of COVID-19 disease was reproduced in the MASCp36 infected mouse model where more severe symptoms were observed in aged mice when compared to young mice. Different from H1N1 pandemic(*32*), COVID-19 appears to have a mild effect on populations under 30 years, and the elderly are more likely to progress to severe disease and are admitted to intensive care unit (ICU) worldwide (*33*). ACE2, the functional receptor of SARS-CoV-2, expressed increasingly in the lungs with age, which might provide an explanation to the higher disease severity observed in older patients with COVID-19 (*34*). More importantly, the host immune response may determine the outcome of the disease. Our immune system is composed of innate immunity and adaptive immunity. The innate immunity comprises of the first line of defense against pathogens and is acute as well as short lived. However, aging is linked with insufficient, prolonged and chronic activation of innate immunity

bioRxiv preprint doi: https://doi.org/10.1101/2020.11.10.377333; this version posted November 11, 2020. The copyright holder for this preprint (which was not certified by peer review) is the author/funder, who has granted bioRxiv a license to display the preprint in perpetuity. It is made available under aCC-BY-NC-ND 4.0 International license.

associated with low-grade and systemic increases in inflammation (inflamm-aging) which can be detrimental for the body (*35*). The delicate co-operation and balance are interrupted by the chronic activation of innate immunity and declined adaptive immune responses with increasing age in COVID-19 (*36*). In the MASCp36 infected mouse model, the young mice presented acute inflammatory response with more innate immune cells infiltration on day 1, while lagged and sustained immune response in aged mice. The different immune response in mice model may be vital in limiting virus replication at early times and contribute to different outcome on day 4 in young or aged mice.

In addition to the age-related skewed distribution of COVID-19, gender-related differences in distribution of COVID-19 disease is also recapitulated in this MASCp36 infected mouse model with increased susceptibility and enhanced pathogenicity observed in male mice when compared to their female counterparts. Biological sex is an important determinant of COVID-19 disease severity (*37*). In China, the death rate among confirmed cases is 2.8% for women and 4.7% for men (*34*). In Italy, half of the confirmed COVID-19 cases are men which account for 65% of all deaths (*38*). This pattern is generally consistent around the world. The skewed distribution of COVID-19 suggests that physiological differences between male and female may cause differential response to infection. So the hypothesis that females display reduced susceptibility to viral infections may be due to the stronger immune responses they mount than males (*39*). It has been studied that androgens may lower and estrogens may enhance several aspects of host immunity. In addition, androgens facilitate and estrogens suppress lymphocyte apoptosis. Furthermore, genes on the X chromosome important for regulating immune functions, and androgens may suppress the expression of disease resistance genes such as the immunoglobulin superfamily (*40*). In the MASCp36 infected mouse model, we found out that it presented higher mortality of the male than the female infected with the same dose of virus, indicating the successful recapitulation of COVID-19 and also its potential application in the study of the pathogenesis of the disease.

Learning from SARS-CoV MA15 with increased virulence in mice, multiple gene products may contribute independently to the virulence. Unlike the SARS-CoV MA15, three subsequent emerged mutations (N501Y, K417N, and Q493H) in the MASCp36 were located in RBD, which breaks a barrier for cross-species transmissions of SARS-

bioRxiv preprint doi: https://doi.org/10.1101/2020.11.10.377333; this version posted November 11, 2020. The copyright holder for this preprint (which was not certified by peer review) is the author/funder, who has granted bioRxiv a license to display the preprint in perpetuity. It is made available under aCC-BY-NC-ND 4.0 International license.

CoV-2, enabling gradually adapted recognition of SARS-CoV-2 to mACE2 during the *in vivo* passages in mice. The serially increased affinities between mACE2 and the RBD of mouse-adapted strains confer to enhanced infections in mice. Cryo-EM structures of the mACE2 in complex with $RBD_{MASCp25}$ and $RBD_{MASCp36}$ define preciously the atomic determinants of the receptor-binding switch, providing novel insights into adaptation-mediated evolution and cross-transmission of SARS-CoV-2. In addition, there are also 9 amino acid substitutions outside the S protein of MASCp36 (Fig. S8). At present, we cannot rule out the contribution of these mutations, and further validation with reverse genetic tools will help understand the biological function of each single mutation (41).

In conclusion, our MASCp36 mouse model exhibited symptoms of DAD and even developed ARDS in both laboratory standard BALB/c and C57BL/6 rodent model, which largely simulated COVID-19 severe disease. And the age and gender-dependent mortality well reproduced the clinical findings of human COVID-19. This novel model will be of high value for studying the pathogenesis of COVID-19 with genetic modified mice and for the rapid efficacy tests of potent countermeasures against SARS-CoV-2.

References and Notes:

1. L. F. Moriarty, M. M. Plucinski, B. J. Marston, E. V. Kurbatova, B. Knust, E. L. Murray, N. Pesik, D. Rose, D. Fitter, M. Kobayashi, M. Toda, P. T. Cantey, T. Scheuer, E. S. Halsey, N. J. Cohen, L. Stockman, D. A. Wadford, A. M. Medley, G. Green, J. J. Regan, K. Tardivel, S. White, C. Brown, C. Morales, C. Yen, B. Wittry, A. Freeland, S. Naramore, R. T. Novak, D. Daigle, M. Weinberg, A. Acosta, C. Herzig, B. K. Kapella, K. R. Jacobson, K. Lamba, A. Ishizumi, J. Sarisky, E. Svendsen, T. Blocher, C. Wu, J. Charles, R. Wagner, A. Stewart, P. S. Mead, E. Kurylo, S. Campbell, R. Murray, P. Weidle, M. Cetron, C. R. Friedman, C. D. C. C. S. R. Team, C.-T. California Department of Public Health, C.-T. Solano County, Public Health Responses to COVID-19 Outbreaks on Cruise Ships - Worldwide, February-March 2020. MMWR. Morbidity and mortality weekly report 69, 347-352 (2020); published online EpubMar 27 (10.15585/mmwr.mm6912e3).
2. C. Edler, A. S. Schroder, M. Aepfelbacher, A. Fitzek, A. Heinemann, F. Heinrich, A. Klein, F. Langenwalder, M. Lutgehetmann, K. Meissner, K. Puschel, J. Schadler, S. Steurer, H. Mushumba, J. P. Sperhake, Dying with SARS-CoV-2 infection-an autopsy study of the first consecutive 80 cases in Hamburg, Germany. International journal of legal medicine 134, 1275-1284 (2020); published online EpubJul (10.1007/s00414-020-02317-w).
3. B. Hanley, S. B. Lucas, E. Youd, B. Swift, M. Osborn, Autopsy in suspected COVID-19 cases. Journal of clinical pathology 73, 239-242 (2020); published online EpubMay (10.1136/jclinpath-2020-206522).
4. B. Zhou, W. Zhao, R. Feng, X. Zhang, X. Li, Y. Zhou, L. Peng, Y. Li, J. Zhang, J. Luo, L. Li, J. Wu, C. Yang, M. Wang, Y. Zhao, K. Wang, H. Yu, Q. Peng, N. Jiang, The pathological

bioRxiv preprint doi: https://doi.org/10.1101/2020.11.10.377333; this version posted November 11, 2020. The copyright holder for this preprint (which was not certified by peer review) is the author/funder, who has granted bioRxiv a license to display the preprint in perpetuity. It is made available under aCC-BY-NC-ND 4.0 International license.

autopsy of coronavirus disease 2019 (COVID-2019) in China: a review. Pathogens and disease 78, (2020); published online EpubApr 1 (10.1093/femspd/ftaa026).

5. E. P. Scully, J. Haverfield, R. L. Ursin, C. Tannenbaum, S. L. Klein, Considering how biological sex impacts immune responses and COVID-19 outcomes. Nature reviews. Immunology 20, 442-447 (2020); published online EpubJul (10.1038/s41577-020-0348-8).
6. K. Liu, Y. Chen, R. Lin, K. Han, Clinical features of COVID-19 in elderly patients: A comparison with young and middle-aged patients. The Journal of infection 80, e14-e18 (2020); published online EpubJun (10.1016/j.jinf.2020.03.005).
7. J. Lan, J. Ge, J. Yu, S. Shan, H. Zhou, S. Fan, Q. Zhang, X. Shi, Q. Wang, L. Zhang, X. Wang, Structure of the SARS-CoV-2 spike receptor-binding domain bound to the ACE2 receptor. Nature 581, 215-220 (2020); published online EpubMay (10.1038/s41586-020-2180-5).
8. B. Hu, H. Guo, P. Zhou, Z. L. Shi, Characteristics of SARS-CoV-2 and COVID-19. Nature reviews. Microbiology, (2020); published online EpubOct 6 (10.1038/s41579-020-00459-7).
9. W. Ren, G. Hu, X. Zhao, Y. Wang, H. Shi, J. Lan, Y. Zhu, J. Wu, D. J. Kenney, D. Florian, Y. Tong, J. Zhong, Y. Xie, X. Wang, Z. Yuan, D. Zhou, R. Zhang, Q. Ding, Comparative analysis reveals the species-specific genetic determinants of ACE2 required for SARS-CoV-2 entry. bioRxiv, 2020.2009.2020.297242 (2020)10.1101/2020.09.20.297242).
10. L. Bao, W. Deng, B. Huang, H. Gao, J. Liu, L. Ren, Q. Wei, P. Yu, Y. Xu, F. Qi, Y. Qu, F. Li, Q. Lv, W. Wang, J. Xue, S. Gong, M. Liu, G. Wang, S. Wang, Z. Song, L. Zhao, P. Liu, L. Zhao, F. Ye, H. Wang, W. Zhou, N. Zhu, W. Zhen, H. Yu, X. Zhang, L. Guo, L. Chen, C. Wang, Y. Wang, X. Wang, Y. Xiao, Q. Sun, H. Liu, F. Zhu, C. Ma, L. Yan, M. Yang, J. Han, W. Xu, W. Tan, X. Peng, Q. Jin, G. Wu, C. Qin, The pathogenicity of SARS-CoV-2 in hACE2 transgenic mice. Nature 583, 830-833 (2020); published online EpubJul (10.1038/s41586-020-2312-y).
11. B. Israelow, E. Song, T. Mao, P. Lu, A. Meir, F. Liu, M. M. Alfajaro, J. Wei, H. Dong, R. J. Homer, A. Ring, C. B. Wilen, A. Iwasaki, Mouse model of SARS-CoV-2 reveals inflammatory role of type I interferon signaling. bioRxiv, (2020); published online EpubMay 27 (10.1101/2020.05.27.118893).
12. A. O. Hassan, J. B. Case, E. S. Winkler, L. B. Thackray, N. M. Kafai, A. L. Bailey, B. T. McCune, J. M. Fox, R. E. Chen, W. B. Alsoussi, J. S. Turner, A. J. Schmitz, T. Lei, S. Shrihari, S. P. Keeler, D. H. Fremont, S. Greco, P. B. McCray, Jr., S. Perlman, M. J. Holtzman, A. H. Ellebedy, M. S. Diamond, A SARS-CoV-2 Infection Model in Mice Demonstrates Protection by Neutralizing Antibodies. Cell 182, 744-753 e744 (2020); published online EpubAug 6 (10.1016/j.cell.2020.06.011).
13. K. H. Dinnon, 3rd, S. R. Leist, A. Schafer, C. E. Edwards, D. R. Martinez, S. A. Montgomery, A. West, B. L. Yount, Jr., Y. J. Hou, L. E. Adams, K. L. Gully, A. J. Brown, E. Huang, M. D. Bryant, I. C. Choong, J. S. Glenn, L. E. Gralinski, T. P. Sheahan, R. S. Baric, A mouse-adapted model of SARS-CoV-2 to test COVID-19 countermeasures. Nature 586, 560-566 (2020); published online EpubOct (10.1038/s41586-020-2708-8).
14. H. Gu, Q. Chen, Adaptation of SARS-CoV-2 in BALB/c mice for testing vaccine efficacy. 369, 1603-1607 (2020); published online EpubSep 25 (10.1126/science.abc4730).

bioRxiv preprint doi: https://doi.org/10.1101/2020.11.10.377333; this version posted November 11, 2020. The copyright holder for this preprint (which was not certified by peer review) is the author/funder, who has granted bioRxiv a license to display the preprint in perpetuity. It is made available under aCC-BY-NC-ND 4.0 International license.

15. S. R. Leist, K. H. Dinnon, 3rd, A. Schäfer, L. V. Tse, K. Okuda, Y. J. Hou, A. West, C. E. Edwards, W. Sanders, E. J. Fritch, K. L. Gully, T. Scobey, A. J. Brown, T. P. Sheahan, N. J. Moorman, R. C. Boucher, L. E. Gralinski, S. A. Montgomery, R. S. Baric, A Mouse-Adapted SARS-CoV-2 Induces Acute Lung Injury and Mortality in Standard Laboratory Mice. Cell, (2020); published online EpubSep 23 (10.1016/j.cell.2020.09.050).
16. H. Gu, Q. Chen, G. Yang, L. He, H. Fan, Y. Q. Deng, Y. Wang, Y. Teng, Z. Zhao, Y. Cui, Y. Li, X. F. Li, J. Li, N. N. Zhang, X. Yang, S. Chen, Y. Guo, G. Zhao, X. Wang, D. Y. Luo, H. Wang, X. Yang, Y. Li, G. Han, Y. He, X. Zhou, S. Geng, X. Sheng, S. Jiang, S. Sun, C. F. Qin, Y. Zhou, Adaptation of SARS-CoV-2 in BALB/c mice for testing vaccine efficacy. Science 369, 1603-1607 (2020); published online EpubSep 25 (10.1126/science.abc4730).
17. G. Matute-Bello, G. Downey, B. B. Moore, S. D. Groshong, M. A. Matthay, A. S. Slutsky, W. M. Kuebler, An official American Thoracic Society workshop report: features and measurements of experimental acute lung injury in animals. American journal of respiratory cell and molecular biology 44, 725-738 (2011); published online EpubMay (10.1165/rcmb.2009-0210ST).
18. P. F. Canete, C. G. Vinuesa, COVID-19 Makes B Cells Forget, but T Cells Remember. Cell 183, 13-15 (2020); published online EpubOct 1 (10.1016/j.cell.2020.09.013).
19. y. chen, Z. Feng, B. Diao, R. Wang, G. Wang, C. Wang, Y. Tan, L. Liu, C. Wang, Y. Liu, Y. Liu, Z. Yuan, L. Ren, Y. Wu, The Novel Severe Acute Respiratory Syndrome Coronavirus 2 (SARS-CoV-2) Directly Decimates Human Spleens and Lymph Nodes. medRxiv, 2020.2003.2027.20045427 (2020)10.1101/2020.03.27.20045427).
20. B. Diao, C. Wang, R. Wang, Z. Feng, Y. Tan, H. Wang, C. Wang, L. Liu, Y. Liu, Y. Liu, G. Wang, Z. Yuan, L. Ren, Y. Wu, Y. Chen, Human Kidney is a Target for Novel Severe Acute Respiratory Syndrome Coronavirus 2 (SARS-CoV-2) Infection. medRxiv, 2020.2003.2004.20031120 (2020)10.1101/2020.03.04.20031120).
21. Z. Lv, Y. Q. Deng, Q. Ye, L. Cao, C. Y. Sun, C. Fan, W. Huang, S. Sun, Y. Sun, L. Zhu, Q. Chen, N. Wang, J. Nie, Z. Cui, D. Zhu, N. Shaw, X. F. Li, Q. Li, L. Xie, Y. Wang, Z. Rao, C. F. Qin, X. Wang, Structural basis for neutralization of SARS-CoV-2 and SARS-CoV by a potent therapeutic antibody. Science 369, 1505-1509 (2020); published online EpubSep 18 (10.1126/science.abc5881).
22. J. Wang, L. Shuai, Mouse-adapted SARS-CoV-2 replicates efficiently in the upper and lower respiratory tract of BALB/c and C57BL/6J mice. 11, 776-782 (2020); published online EpubOct (10.1007/s13238-020-00767-x).
23. K. H. Dinnon, 3rd, S. R. Leist, A. Schäfer, C. E. Edwards, A mouse-adapted model of SARS-CoV-2 to test COVID-19 countermeasures. 586, 560-566 (2020); published online EpubOct (10.1038/s41586-020-2708-8).
24. B. T. Bradley, H. Maioli, R. Johnston, I. Chaudhry, S. L. Fink, H. Xu, B. Najafian, G. Deutsch, J. M. Lacy, T. Williams, N. Yarid, D. A. Marshall, Histopathology and ultrastructural findings of fatal COVID-19 infections in Washington State: a case series. Lancet 396, 320-332 (2020); published online EpubAug 1 (10.1016/S0140-6736(20)31305-2).
25. S. Tian, Y. Xiong, H. Liu, L. Niu, J. Guo, M. Liao, S. Y. Xiao, Pathological study of the 2019 novel coronavirus disease (COVID-19) through postmortem core biopsies. Modern

bioRxiv preprint doi: https://doi.org/10.1101/2020.11.10.377333; this version posted November 11, 2020. The copyright holder for this preprint (which was not certified by peer review) is the author/funder, who has granted bioRxiv a license to display the preprint in perpetuity. It is made available under aCC-BY-NC-ND 4.0 International license.

pathology : an official journal of the United States and Canadian Academy of Pathology, Inc 33, 1007-1014 (2020); published online EpubJun (10.1038/s41379-020-0536-x).

26. A. Kumar, A. Arora, P. Sharma, S. A. Anikhindi, N. Bansal, V. Singla, S. Khare, A. Srivastava, Clinical Features of COVID-19 and Factors Associated with Severe Clinical Course: A Systematic Review and Meta-Analysis. Ssrn, 3566166 (2020); published online EpubApr 21 (10.2139/ssrn.3566166).
27. Z. Xu, L. Shi, Y. Wang, J. Zhang, L. Huang, C. Zhang, S. Liu, P. Zhao, H. Liu, L. Zhu, Y. Tai, C. Bai, T. Gao, J. Song, P. Xia, J. Dong, J. Zhao, F. S. Wang, Pathological findings of COVID-19 associated with acute respiratory distress syndrome. The Lancet. Respiratory medicine 8, 420-422 (2020); published online EpubApr (10.1016/S2213-2600(20)30076-X).
28. X. W. Pan, D. Xu, H. Zhang, W. Zhou, L. H. Wang, X. G. Cui, Identification of a potential mechanism of acute kidney injury during the COVID-19 outbreak: a study based on single-cell transcriptome analysis. Intensive care medicine 46, 1114-1116 (2020); published online EpubJun (10.1007/s00134-020-06026-1).
29. M. A. Ellul, L. Benjamin, B. Singh, S. Lant, B. D. Michael, A. Easton, R. Kneen, S. Defres, J. Sejvar, T. Solomon, Neurological associations of COVID-19. The Lancet. Neurology 19, 767-783 (2020); published online EpubSep (10.1016/S1474-4422(20)30221-0).
30. J. M. Nicholls, L. L. Poon, K. C. Lee, W. F. Ng, S. T. Lai, C. Y. Leung, C. M. Chu, P. K. Hui, K. L. Mak, W. Lim, K. W. Yan, K. H. Chan, N. C. Tsang, Y. Guan, K. Y. Yuen, J. S. Peiris, Lung pathology of fatal severe acute respiratory syndrome. Lancet 361, 1773-1778 (2003); published online EpubMay 24 (10.1016/s0140-6736(03)13413-7).
31. F. Wu, S. Zhao, B. Yu, Y. M. Chen, W. Wang, Z. G. Song, Y. Hu, Z. W. Tao, J. H. Tian, Y. Y. Pei, M. L. Yuan, Y. L. Zhang, F. H. Dai, Y. Liu, Q. M. Wang, J. J. Zheng, L. Xu, E. C. Holmes, Y. Z. Zhang, A new coronavirus associated with human respiratory disease in China. Nature 579, 265-269 (2020); published online EpubMar (10.1038/s41586-020-2008-3).
32. H. V. Fineberg, Pandemic preparedness and response--lessons from the H1N1 influenza of 2009. The New England journal of medicine 370, 1335-1342 (2014); published online EpubApr 3 (10.1056/NEJMra1208802).
33. World Health Organization, (WHO), “Report of the WHO-China Joint Mission on Coronavirus Disease 2019 (COVID-19)”, 2020, [https://www.who.int/docs/default-source/coronaviruse/who-china-joint-mission-on-covid-19-final-report.pdf.]
34. Y. Chen, L. Li, SARS-CoV-2: virus dynamics and host response. The Lancet. Infectious diseases 20, 515-516 (2020); published online EpubMay (10.1016/S1473-3099(20)30235-8).
35. D. Furman, J. Campisi, E. Verdin, P. Carrera-Bastos, S. Targ, C. Franceschi, L. Ferrucci, D. W. Gilroy, A. Fasano, G. W. Miller, A. H. Miller, A. Mantovani, C. M. Weyand, N. Barzilai, J. J. Goronzy, T. A. Rando, R. B. Effros, A. Lucia, N. Kleinstreuer, G. M. Slavich, Chronic inflammation in the etiology of disease across the life span. Nature medicine 25, 1822-1832 (2019); published online EpubDec (10.1038/s41591-019-0675-0).
36. M. Tan, Y. Liu, R. Zhou, X. Deng, F. Li, K. Liang, Y. Shi, Immunopathological characteristics of coronavirus disease 2019 cases in Guangzhou, China. Immunology 160, 261-268 (2020); published online EpubJul (10.1111/imm.13223).

bioRxiv preprint doi: https://doi.org/10.1101/2020.11.10.377333; this version posted November 11, 2020. The copyright holder for this preprint (which was not certified by peer review) is the author/funder, who has granted bioRxiv a license to display the preprint in perpetuity. It is made available under aCC-BY-NC-ND 4.0 International license.

37. J. P. Dudley, N. T. Lee, Disparities in Age-specific Morbidity and Mortality From SARS-CoV-2 in China and the Republic of Korea. Clinical infectious diseases : an official publication of the Infectious Diseases Society of America 71, 863-865 (2020); published online EpubJul 28 (10.1093/cid/ciaa354).
38. Epicentro L'epidemiologia per la sanità pubblica Istituto Superiore di Sanità, "Characteristics of COVID-19 patients dying in Italy Report based on available data on March 20th, 2020", 2020, [https://www.epicentro.iss.it/coronavirus/bollettino/Report-COVID-2019_20_marzo_eng.pdf.]
39. E. J. Marquez, J. Trowbridge, G. A. Kuchel, J. Banchereau, D. Ucar, The lethal sex gap: COVID-19. Immunity & ageing : I & A 17, 13 (2020)10.1186/s12979-020-00183-z).
40. S. L. Klein, K. L. Flanagan, Sex differences in immune responses. Nature reviews. Immunology 16, 626-638 (2016); published online EpubOct (10.1038/nri.2016.90).
41. J. A. Plante, Y. Liu, J. Liu, H. Xia, Spike mutation D614G alters SARS-CoV-2 fitness. (2020); published online EpubOct 26 (10.1038/s41586-020-2895-3).

Acknowledgements: This work was in memory of Prof. Yusen Zhou. We thank Dr. X.D. Yu and Dr. J.J. Zhao for excellent technical and biosafety support. This work was supported by the National Key Plan for Scientific Research and Development of China (No.2016YFD0500306, 2020YFC0841100, 2020YFC0840900, 2020YFA0707500, 2018YFA0900801), the National Science and Technology Major Project of China (No.2017ZX10304402003) and the Strategic Priority Research Program (XDB29010000, XDB37030000). Cheng-Fng Qin was supported by the National Science Fund for Distinguished Young Scholar (No. 81925025), and the Innovative Research Group (No. 81621005) from the NSFC, and the Innovation Fund for Medical Sciences (No.2019RU040) from the Chinese Academy of Medical Sciences (CAMS). Xiangxi Wang was supported by Ten Thousand Talent Program and the NSFS Innovative Research Group (No. 81921005).

Author contributions: S.S., H.G., C.L., C.Q., Y.G., L.R., F.H., Y.Q., D.Q., S.X, Q.Y., L.M., L.J., F.R., W.L., Z.Y., Z.C., Z.L., C.Y., Y.G., S.Q., and S.M. performed experiments; S.S., H.G., C.Q., Y.G., L.R., F.H, C.Y., Y.X. and H.W. analyzed data. C.-F.Q., H.G., and S.S conceived the project and designed the experiments. S.S. and H.G., and R.T.L. wrote the draft of the manuscript. C.-F.Q., and X.W. supervised the study and wrote the manuscript with the input of all co-authors.

Competing interests: All authors have no competing interests

Data and materials availability: All requests for resources and reagents should be directed to C.-

bioRxiv preprint doi: https://doi.org/10.1101/2020.11.10.377333; this version posted November 11, 2020. The copyright holder for this preprint (which was not certified by peer review) is the author/funder, who has granted bioRxiv a license to display the preprint in perpetuity. It is made available under aCC-BY-NC-ND 4.0 International license.

F.Q. (qincf@bmi.ac.cn and qinlab313@163.com) and will be fulfilled after completion of a materials transfer agreement.

bioRxiv preprint doi: https://doi.org/10.1101/2020.11.10.377333; this version posted November 11, 2020. The copyright holder for this preprint (which was not certified by peer review) is the author/funder, who has granted bioRxiv a license to display the preprint in perpetuity. It is made available under aCC-BY-NC-ND 4.0 International license.

Figure legends

Figure 1

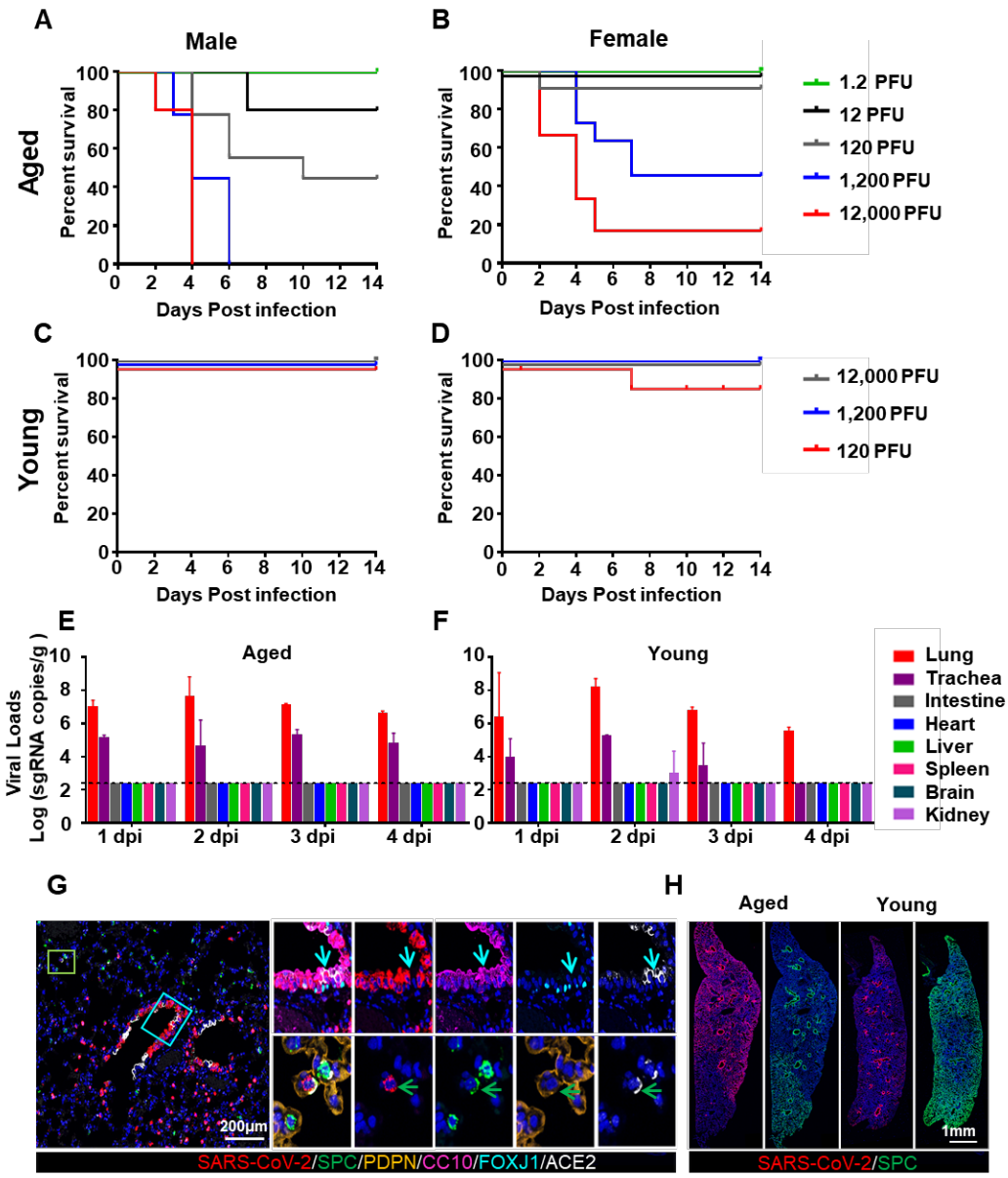

Figure 1. MASCp36 is highly virulent in aged mice. (A-D) Survival curve of BALB/c mice upon challenge with MASCp36. Group of female or male aged BALB/c mice (9-month-old), or young BALB/c mice (8-week-old) were infected intranasally with the indicated doses of MASCp36, and the clinical symptoms and mortality were recorded for 14 days (n=6 per group). (E-F) Tissue distribution of SARS-CoV-2 viral RNAs in mice infected with MASCp36. Groups of aged and young BALB/c mice were i.n. inoculated with 12,000 PFU of MASCp36, and sacrificed at 4 dpi. All the indicated tissue samples were collected and subjected to viral subgenomic RNA load analysis by

bioRxiv preprint doi: https://doi.org/10.1101/2020.11.10.377333; this version posted November 11, 2020. The copyright holder for this preprint (which was not certified by peer review) is the author/funder, who has granted bioRxiv a license to display the preprint in perpetuity. It is made available under aCC-BY-NC-ND 4.0 International license.

RT-qPCR. Dash lines denote the detection limit. Data are presented as means ± SEM (n=4 per group). (G) Multiplex immunofluorescence staining for detection of SARS-CoV-2 targeted cells in lung sections of aged mouse at 1 dpi. SARS-CoV-2 N protein (red), ACE2 (white), SPC (green), PDPN (gold), CC10 (magenta), FOXJ1 (cyan). The framed areas are shown adjacently at a higher magnification.(H) Multiplex immunofluorescence staining of mouse lung sections for SARS-CoV-2 N protein (red) and SPC (green) detection in aged and young mice at 1 dpi.

bioRxiv preprint doi: https://doi.org/10.1101/2020.11.10.377333; this version posted November 11, 2020. The copyright holder for this preprint (which was not certified by peer review) is the author/funder, who has granted bioRxiv a license to display the preprint in perpetuity. It is made available under aCC-BY-NC-ND 4.0 International license.

Figure 2

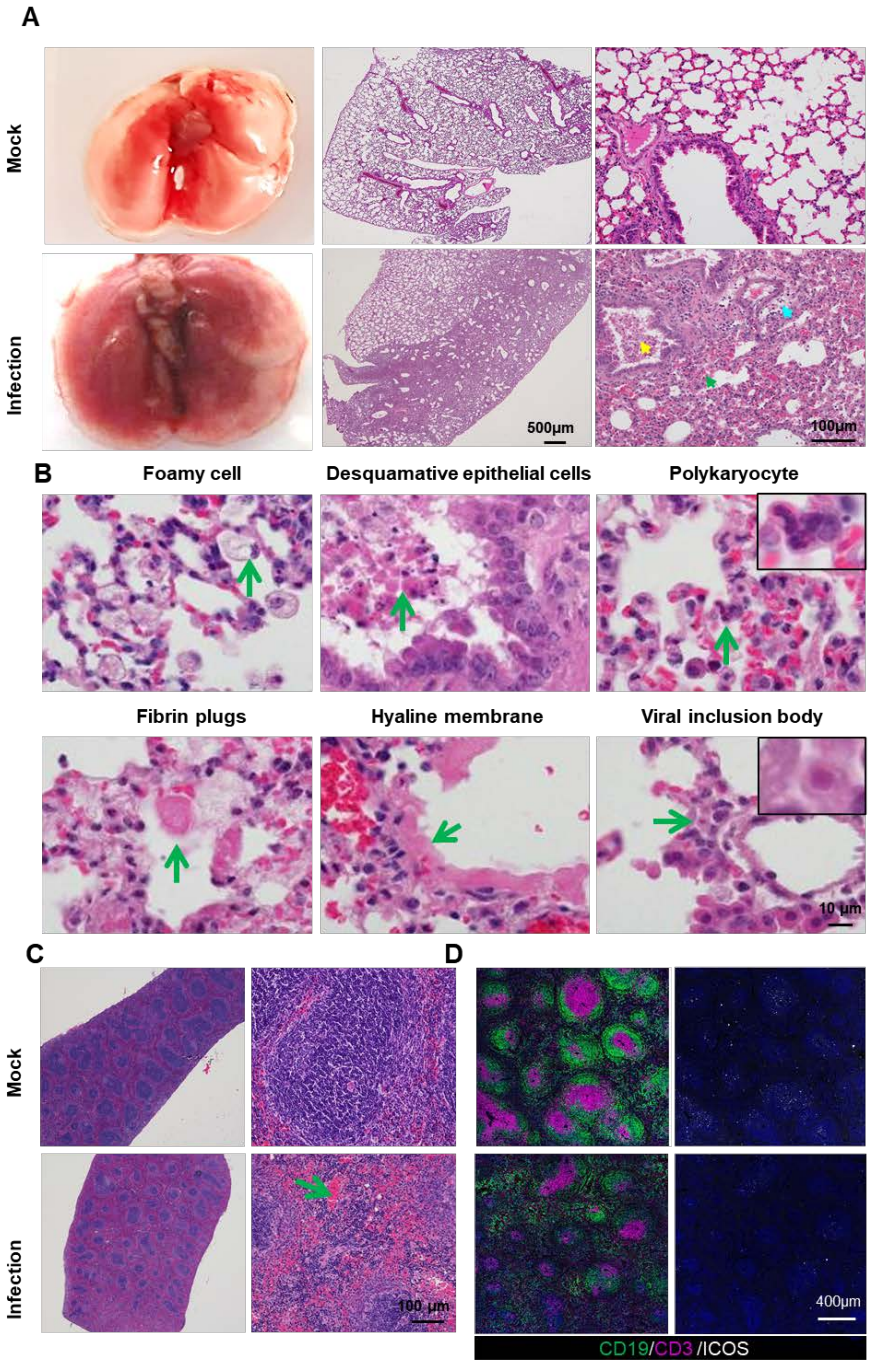

Figure 2. Multi-organ damage during BALB/c mice infection with MASCp36 (A) Gross necropsy and hematoxylin and eosin (H&E) staining of lung sections from aged (9-month-old) BALB/c mice infected with MASCp36. (n=3 per group). (B) Microscopic observation of lungs showing foamy cells, desquamative epithelial cells, polykaryocytes, fibrin plugs, hyaline membrane and viral inclusion body. (C)

bioRxiv preprint doi: https://doi.org/10.1101/2020.11.10.377333; this version posted November 11, 2020. The copyright holder for this preprint (which was not certified by peer review) is the author/funder, who has granted bioRxiv a license to display the preprint in perpetuity. It is made available under aCC-BY-NC-ND 4.0 International license.

Hematoxylin and eosin (H&E) staining of spleen sections from aged BALB/c mice infected with MASCp36. (D) Multiplex immunofluorescence staining of mouse spleen sections for detection of CD19 (green) B cells, CD3 (magenta) T cells and ICOS (white) follicular helper T cells.

bioRxiv preprint doi: https://doi.org/10.1101/2020.11.10.377333; this version posted November 11, 2020. The copyright holder for this preprint (which was not certified by peer review) is the author/funder, who has granted bioRxiv a license to display the preprint in perpetuity. It is made available under aCC-BY-NC-ND 4.0 International license.

Figure 3

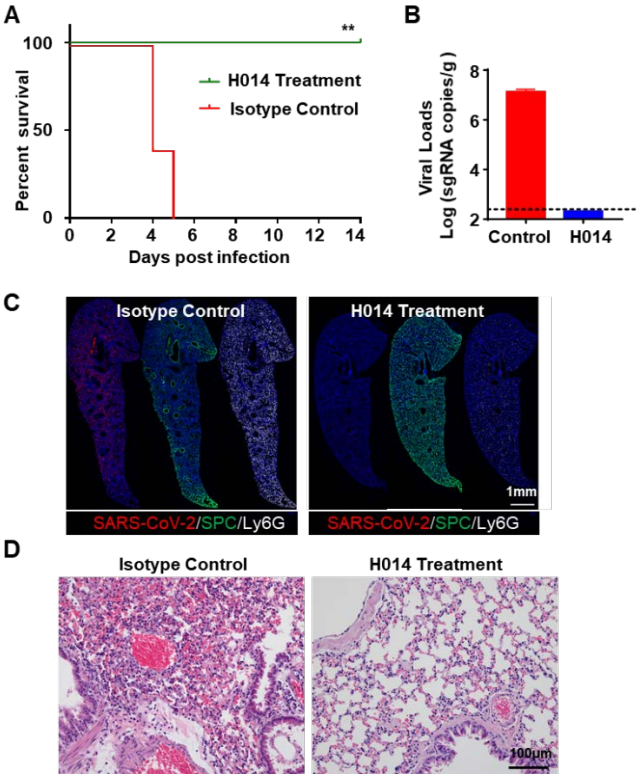

Figure 3. The efficacy of H014 against MASCp36 infection. Male aged BALB/c mice (9-month-old) infected with 12,000PFU of MASCp36. (A) survival curves of mice in H014 and mock treatment groups (n=5 per group). Statistical significance was analyzed by Student's t test. (B) Lung samples were collected and subjected to viral RNA load analysis by RT-qPCR. Dash lines denote the detection limit. (n=3 per group) (C) Multiplex immunofluorescence staining of mouse lung sections for detection of SARS-CoV-2 N protein (red), SPC (green) and Ly6G (white) (D) Hematoxylin and eosin (H&E) staining of lung sections from H014 or isotype control (n=3 per group).

bioRxiv preprint doi: https://doi.org/10.1101/2020.11.10.377333; this version posted November 11, 2020. The copyright holder for this preprint (which was not certified by peer review) is the author/funder, who has granted bioRxiv a license to display the preprint in perpetuity. It is made available under aCC-BY-NC-ND 4.0 International license.

Figure 4

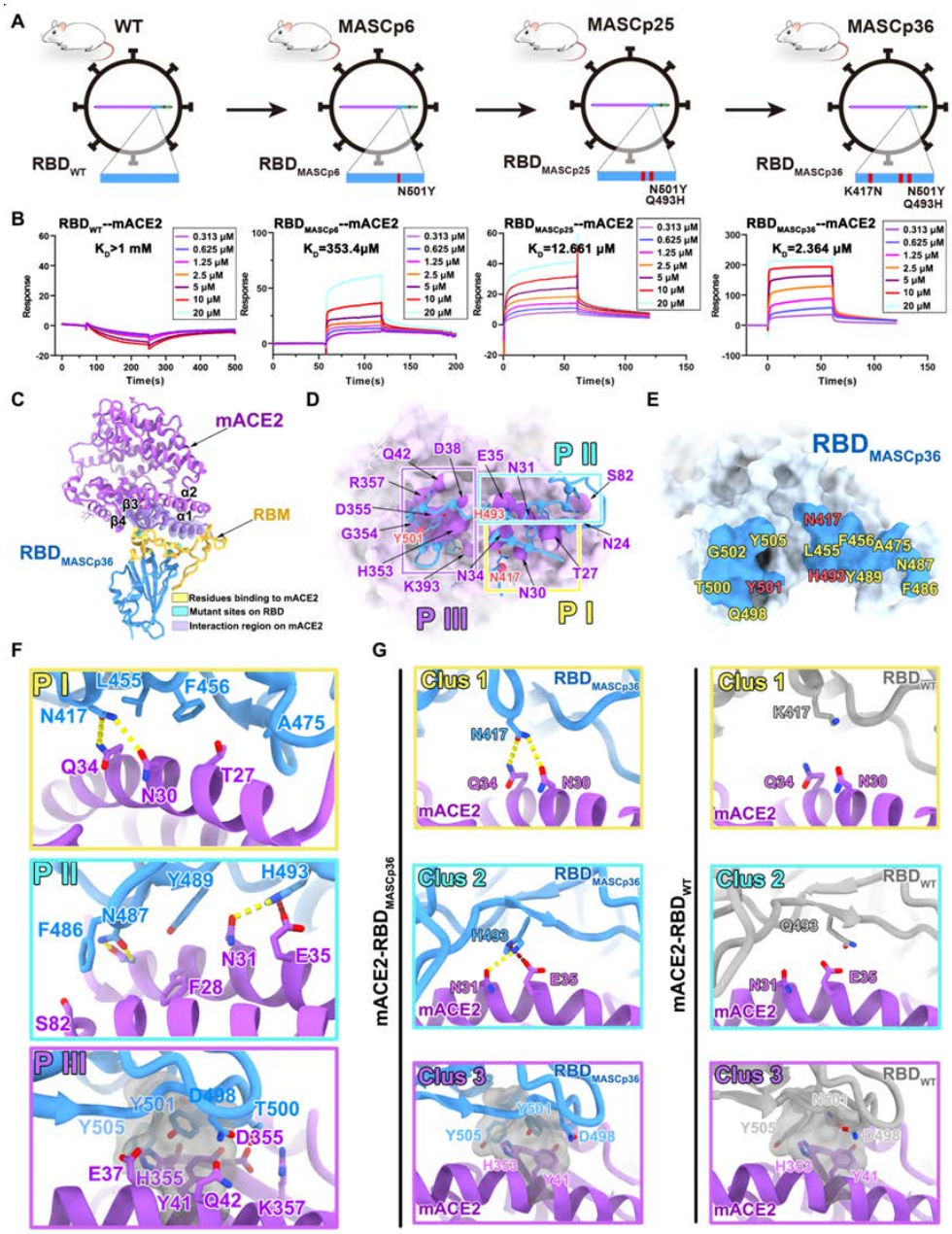

Fig4. Mechanism of binding of SARS-CoV-2 derived MASCp36 to mACE2 (A) Schematic diagram depicting virus harboring different RBD mutations. The mutation site is marked with a red rectangle. (B) Binding properties of RBD_{WT}, RBD_{MASCp6}, $RBD_{MASCp25}$ and $RBD_{MASCp36}$ to mACE2 analyzed using SPR. For both panels, mACE2 was loaded onto the sensor; RBD_{WT}, RBD_{MASCp6}, $RBD_{MASCp25}$ and $RBD_{MASCp36}$ were injected. Response units were plotted against protein concentrations. The K_D values

bioRxiv preprint doi: https://doi.org/10.1101/2020.11.10.377333; this version posted November 11, 2020. The copyright holder for this preprint (which was not certified by peer review) is the author/funder, who has granted bioRxiv a license to display the preprint in perpetuity. It is made available under aCC-BY-NC-ND 4.0 International license.

were calculated by BIAcore® 3000 analysis software (BIAevaluation version 4.1). (C) Overall structure of $RBD_{MASCp36}$ bound to mACE2. Residues of $RBD_{MASCp36}$ participating in the binding to mACE2 are shown as spheres and colored in yellow, the mutation sites are colored in cyan, the RBM is colored in gold. The region of mACE2 responsible for binding is labelled. (D and E) The binding interface between $RBD_{MASCp36}$ and mACE2. The residues involved in binding to mACE2 are presented as sticks, and the residues of mACE2 interacting with $RBD_{MASCp36}$ are shown as surface. The mutated residues in $RBD_{MASCp36}$ are colored in red. (F) Details of the interactions between $RBD_{MASCp36}$ and mACE2. Some residues involved in the formation of hydrophobic patches (grey mesh), salt bridge (red dash) and hydrogen bonds (yellow dash) are shown as sticks and labeled. (G) The comparison of interactions at RBD_{WT}-mACE2 and $RBD_{MASCp36}$-mACE2 interface. RBD_{WT}, $RBD_{MASCp36}$ and mACE2 are colored in grey, cyan and purple, respectively. The residues involved in the formation of hydrophobic patches (grey mesh), salt bridge (red dash) and hydrogen bonds (yellow dash) are shown as sticks and labeled.

bioRxiv preprint doi: https://doi.org/10.1101/2020.11.10.377333; this version posted November 11, 2020. The copyright holder for this preprint (which was not certified by peer review) is the author/funder, who has granted bioRxiv a license to display the preprint in perpetuity. It is made available under aCC-BY-NC-ND 4.0 International license.

Supplementary Materials for

Characterization and structural basis of a lethal mouse-adapted SARS-CoV-2

Shihui Sun[1†], Hongjing Gu[1†], Lei Cao[2†], Qi Chen[1†], Guan Yang[3†], Rui-Ting Li[1†], Hang Fan[1†], Qing Ye[1], Yong-Qiang Deng[1], Xiaopeng Song[3], Yini,Qi[3], Min Li[1], Jun Lan[2], Rui Feng[2], Lei Wang[2], Yi-Fei Zhang[1], Chao Zhou[1], Lingna Zhao[1], Yuehong Chen[1], Meng Shen[1], Yujun Cui, Xiao Yang[3], Xinquan Wang[4], Hui Wang[1*], Xiangxi Wang[2*], Cheng-Feng Qin[1*]

Correspondence to: Cheng-Feng Qin (qincf@bmi.ac.cn), Xiangxi Wang (xiangxi@ibp.ac.cn), or Hui Wang (geno0109@vip.sina.com)

This PDF file includes:

Materials and Methods

Figs. S1 to S13

Table S1 to S3

References and notes (42 – 49)

Video

bioRxiv preprint doi: https://doi.org/10.1101/2020.11.10.377333; this version posted November 11, 2020. The copyright holder for this preprint (which was not certified by peer review) is the author/funder, who has granted bioRxiv a license to display the preprint in perpetuity. It is made available under aCC-BY-NC-ND 4.0 International license.

Materials and Methods

Ethics statement. All procedures involving infectious virus were conducted in Biosafety Level 3 laboratory (BSL-3) and approved by the Animal Experiment Committee of Laboratory Animal Center, Beijing Institute of Microbiology and Epidemiology (approval number: IACUC-DWZX-2020-002).

Virus and mice. Mouse adapted strain of SARS-CoV-2 (MASCp6) was developed in our previous study (*16*) . Additional serial passage of 30 times was performed as previously described (*16*) . BALB/c and C57BL/6 mice were purchased from Beijing HFK Bioscience Co., LTD and Beijing Vitalriver Laboratory Animal Technology Co. Ltd. The virus stock of MASCp36 was amplified and titrated by standard plaque forming assay on Vero cells.

Measurement of viral sgRNA. Tissue homogenates were clarified by centrifugation at 6,000 rpm for 6 min, and the supernatants were transferred to a new EP tube. RNA was extracted using the QIAamp Viral RNA Mini Kit (Giagen) according to the manufacturer's protocol (*42*). sgRNA quantification in each sample was performed by quantitative reverse transcription PCR (RT-qPCR) targeting the S gene of SARS-CoV-2. RT-qPCR was performed using One Step PrimeScript RT-PCR Kit (Takara, Japan) with the following primers and probes: sgRNA-F (5'-CGATCTCTTGTAGATCTGTTCTC-3'); sgRNA-R (5'- ATATTGCAGCAGTACGCACACA-3'); and sgRNA-P3 (5'- ACACTAGCCATCCTTACTGCGCTTCG-3').

Deep sequencing. Total RNA was extracted after each passage using High Pure Viral RNA Kit (Roche, Switzerland), and the purified viral RNA was used for library construction using Ion Total RNA-Seq kit V2 (Thermo Fisher, USA). The library was sequenced on an Ion Torrent S5Plus sequencer (Thermo Fisher, USA). Sequences were assembled and analyzed with CLC Genomic

bioRxiv preprint doi: https://doi.org/10.1101/2020.11.10.377333; this version posted November 11, 2020. The copyright holder for this preprint (which was not certified by peer review) is the author/funder, who has granted bioRxiv a license to display the preprint in perpetuity. It is made available under aCC-BY-NC-ND 4.0 International license.

Workbench (Qiagen, Germany). All reads were mapped to SARS-CoV-2 reference genome (Wuhan-Hu-1, GenBank accession number MN908947). The consensus sequence was extracted. Single nucleotide variations with variation proportion above 1% were called using this software.

Mouse virulence study. Female and male 6 weeks- and 9 months BALB/c and C57BL/6 mice were maintained in a pathogen-free facility and housed in cages containing sterilized feed and drinking water. Following intraperitoneal (i.p.) anesthetization with sodium pentobarbital, mice were intranasally (i.n.) inoculated with varying doses of MASCp36 or the same volume of PBS for mock infection. Four mice of each group were sacrificed on days 1 and 4 after infection for lung damage study and sgRNA quantification. Clinical manifestation and survival were recorded for 14 days.

Histopathological analysis. Lung, heart, liver, spleen, kidney, brain, intestine and trachea tissues were collected 4 days post infection with MASCp36, and paraffin-embedded in accordance with standard procedure. Sections at 4 μm thickness were stained with hematoxylin and eosin (H&E) and examined by light microscopy and analyzed by two experienced experimental pathologists.

Multiplex immunofluorescent assay. The multiplex immunofluorescence assay was conducted as previously described (*16*). Briefly, the retrieved sections were incubated with primary antibody for 2 h followed by detection using the HRP-conjugated secondary antibody and TSA-dendron-fluorophores (NEON 7-color Allround Discovery Kit for FFPE, Histova Biotechnology, NEFP750). Afterwards, the primary and secondary antibodies were thoroughly eliminated by heating the slides in retrieval/elution buffer (Abcracker®, Histova Biotechnology, ABCFR5L) for 10 sec at 95°C using microwave. In a serial fashion, each antigen was labeled by distinct fluorophores. Multiplex antibody panels applied in this study include: ACE2 (Abcam, ab108252, 1:200); SARS-CoV-2 N protein (Sinobiological, 40143-R004, 1:2000); CC10 (Millipore, 07-623, 1:500), FOXJ1 (Abcam, ab235445, 1:1000), SPC (Abcam, ab211326, 1:500), Cleaved caspase-3 (CST, 9664, 1:300); Ly-6G (CST, 87048, 1:400); CD68 (CST, 97778, 1:300); CD3 (CST, 78588, 1:300); CD19 (Abcam, ab245235, 1:800); ICOS (Abcam, ab224644, 1:200); CD31 (CST, 77699, 1:300). After all the antibodies were detected sequentially, the slides were imaged using the confocal laser scanning microscopy platform Zeiss LSM880. Some data were further processed and statistically analyzed using Bitplane Imaris software (Bitplane AG, Zurich, Switzerland).

bioRxiv preprint doi: https://doi.org/10.1101/2020.11.10.377333; this version posted November 11, 2020. The copyright holder for this preprint (which was not certified by peer review) is the author/funder, who has granted bioRxiv a license to display the preprint in perpetuity. It is made available under aCC-BY-NC-ND 4.0 International license.

Cytokine and chemokines analysis. Cytokines and chemokines in mouse lung homogenates were measured using a Bio-Plex Pro Mouse Cytokine Grp I Panel 31-Plex (Bio-Rad, USA) according to the manufacturer's protocol. The data were collected on Luminex 200 and analyzed by Luminex PONENT (Thermo Fisher, USA).

RNA sequencing and Bioinformatic analyses. Lung homogenates from MASCp36-infected mice or mock treated mice were processed as previously described (*16*) and subjected to RNA-Seq. Total RNA from lung tissue were extracted using TRIzol (Invitrogen, USA) and treated with DNase I (NEB, USA). Sequencing libraries were generated using NEBNext® UltraTM RNA Library Prep Kit for Illumina® (NEB, USA) following the manufacturer's recommendations and index codes were added to attribute sequences to each sample. The clustering of the index-coded samples was performed on a cBot cluster generation system using HiSeq PE Cluster Kit v4-cBot-HS (Illumina) according to the manufacturer's instructions. After cluster generation, the libraries were sequenced on Illumina Novaseq6000 platform and 150 bp paired-end reads were generated. After sequencing, perl script was used to filter the original data (Raw Data) to clean reads by removing contaminated reads for adapters and low-quality reads. Clean reads were aligned to the mouse genome (Mus_musculus GRCm38.99) using Hisat2 v2.1.0. The number of reads mapped to each gene in each sample was counted by HTSeq v0.6.0 and TPM (Transcripts Per Kilobase of exon model per Million mapped reads) was then calculated to estimate the expression level of genes in each sample. DESeq2 v1.6.3 was used for differential gene expression analysis. Genes with padj≤0.05 and |Log2FC| > 1 were identified as differentially expressed genes (DEGs). DEGs were used as query to search for enriched biological processes (Gene ontology BP) using Metascape. Heatmaps of gene expression levels were constructed using heatmap package in R (https://cran.rstudio.com/web/packages/pheatmap/index.html). Dot plots and volcano plots were constructed using ggplot2 (https://ggplot2.tidyverse.org/) package in R.

In vivo efficacy assay with MASCp36 model. Group of 9-month male BALB/c mice were inoculated intranasally with 40 μL MASCp36 (1,200 PFU) and intraperitoneally administered 200 μL of H014 (50 mg/kg) at 24 hours before and after MASCp36 infection. The same volume of an isotype antibody was administrated as control. On day 4 post infection, 3 mice in each group were sacrificed and lung tissues were prepared for pathology analysis and sgRNA quantification. The

bioRxiv preprint doi: https://doi.org/10.1101/2020.11.10.377333; this version posted November 11, 2020. The copyright holder for this preprint (which was not certified by peer review) is the author/funder, who has granted bioRxiv a license to display the preprint in perpetuity. It is made available under aCC-BY-NC-ND 4.0 International license.

other 6 mice in each group were monitored for survival for 14 days.

Protein expression and purification. The cloning and production of SARS-CoV-2 RBD (residues 319-541, GenBank: MN_908947.3), RBD mutants ($RBD_{MASCp25}$: Q493H, N501Y; RBD_{MASCp}36: K417N, Q493H, N501Y) and mACE2 (residues 19-739, GenBank: NM_001130513.1) involved synthesis of the genes followed by subcloning into the mammalian expression vector pCAGGS with a C-terminal 2×StrepTag to facilitate protein purification. Briefly, wtRBD, $RBD_{MASCp25}$, $RBD_{MASCp36}$ and mACE2 were expressed by transient transfection of HEK Expi 293F cells (Gibco, Thermo Fisher) using Polyethylenimine Max Mw 40,000 (Polysciences). The target protein was purified from clarified cell supernatants 3 days post-transfection using StrepTactin resin (IBA). The resulting protein samples were further purified by size-exclusion chromatography using a Superdex G75 10/300 column (GE Healthcare) or a Superdex G200 10/300 Increase column (GE Healthcare) in 20mM HEPES, 200 mM NaCl, pH 7.0.

To purify the final quaternary complex ($RBD_{MASCp25}$/$RBD_{MASCp36}$-Fab_{B8}-Fab_{D14}-mACE2), firstly, the ternary complex ($RBD_{MASCp25}$/$RBD_{MASCp36}$ -Fab_{B8}-Fab_{D14}) was assembled. $RBD_{MASCp25}$ or $RBD_{MASCp36}$ was mixed with Fab_{B8} and Fab_{D14} at the ratio of 1 : 1.2 : 1.2, and incubated for 30 min on ice. The mixture was then subjected to gel filtration chromatography. Fractions containing the ternary complex ($RBD_{MASCp25}$/$RBD_{MASCp36}$-Fab_{B8}-Fab_{D14}) were pooled and concentrated. Then mACE2 was mixed with the ternary complex ($RBD_{MASCp25}$/$RBD_{MASCp36}$-Fab_{B8}-Fab_{D14}) at the ratio of 1 : 1.2 and incubated for 60 min on ice. The mixture was then passed through Superose 6 10/300 column (GE Healthcare). Fractions containing the quaternary complex ($RBD_{MASCp25}$/$RBD_{MASCp36}$-Fab_{B8}-Fab_{D14}-mACE2) were concentrated to 2mg/ml.

Production of Fab fragment. The B8 and D14 Fab fragments (*43*) were generated using a Pierce

bioRxiv preprint doi: https://doi.org/10.1101/2020.11.10.377333; this version posted November 11, 2020. The copyright holder for this preprint (which was not certified by peer review) is the author/funder, who has granted bioRxiv a license to display the preprint in perpetuity. It is made available under aCC-BY-NC-ND 4.0 International license.

FAB preparation Kit (Thermo Scientific). Briefly, the antibody was mixed with immobilized-papain and then digested at 37 ˚C for 3-4 h. The Fab was separated from the Fc fragment and undigested IgGs by protein A affinity column and then concentrated for analysis.

Surface plasmon resonance. mACE2 was immobilized onto a CM5 sensor chip surface using the NHS/EDC method to a level of ~600 response units (RUs) using BIAcore® 3000 (GE Healthcare) and PBS as running buffer (supplemented with 0.05% Tween-20). wtRBD, $RBD_{MASCp25}$ and $RBD_{MASCp36}$, which were purified and diluted, were injected in concentration from high to low. The binding responses were measured, and chip surfaces were regenerated with 10 mM Glycine, pH 1.5 (GE Healthcare). The apparent binding affinity (K_D) for individual antibody was calculated using BIAcore® 3000 Evaluation Software (GE Healthcare).

For the competitive binding assays, the first sample flew over the chip at a rate of 20 ul/min for 120 s, after which the second sample was injected at the same rate for another 120s. All antibodies were evaluated at a saturation concentration of 500 nM, while mACE2 was applied at 1000 nM concentration. All surfaces of chips were regenerated with 10 mM Glycine, pH 1.5 (GE Healthcare). The response units were recorded at room temperature and analyzed using the same software as mentioned above.

Cryo-EM sample preparation and data collection. For Cryo-EM sample preparation, the quaternary complex ($RBD_{MASCp25}$/$RBD_{MASCp36}$-Fab_{B8}-Fab_{D14}-mACE2) was diluted to 0.8 mg/ml. Holy-carbon gold grid (Quantifoil R0.6/1.0 mesh 300) were freshly glow-discharged with a Solarus 950 plasma cleaner (Gatan) for 60s. A 3 μL aliquot of the mixture complex was transferred onto the grids, blotted with filter paper at 22°C and 100% humidity, and plunged into the ethane using a Vitrobot Mark IV (FEI). For $RBD_{MASCp25}$/$RBD_{MASCp36}$-Fab_{B8}-Fab_{D14}-mACE2 complex,

bioRxiv preprint doi: https://doi.org/10.1101/2020.11.10.377333; this version posted November 11, 2020. The copyright holder for this preprint (which was not certified by peer review) is the author/funder, who has granted bioRxiv a license to display the preprint in perpetuity. It is made available under aCC-BY-NC-ND 4.0 International license.

micrographs were collected at 300 kV using a Titan Krios microscope (Thermo Fisher), equipped with a K2 detector (Gatan, Pleasanton, CA), using SerialEM automated data collection software (*43*) Movies (32 frames, each 0.2 s, total dose 60 $e^{-}Å^{-2}$) were recorded at final pixel size of 1.04 Å with a defocus of between -1.25 and -2.7 μm.

Image processing. For $RBD_{MASCp25}$-Fab_{B8}-Fab_{D14}-mACE2 complex, a total of 2,109 micrographs were recorded. For $RBD_{MASCp36}$-Fab_{B8}-Fab_{D14}-mACE2 complex, a total of 2,982 micrographs were recorded. Both sets of the data were processed in the same way. Firstly, the raw data were processed by MotionCor2, which were aligned and averaged into motion-corrected summed images. Then, the defocus value for each micrograph was determined using Gctf. Next, particles were picked and extracted for two-dimensional alignment. The partial well-defined particles were selected for initial model reconstruction in Relion. The initial model was used as a reference for three-dimensional classification. After the refinement and postprocessing, the overall resolution of $RBD_{MASCp36}$-Fab_{B8}-Fab_{D14}-mACE2 complex was up to 3.69Å, on the basis of the gold-standard Fourier shell correlation (threshold = 0.143) (*44*). For $RBD_{MASCp25}$-Fab_{B8}-Fab_{D14}-mACE2 complex, the Class I complex the resolution achieved was 7.89 Å, ClassII complex had a resolution of 8.17 Å, while Class III complex was reconstructed to a resolution of 4.4 Å. The quality of the local resolution was evaluated by ResMap *(45)*.

Model building and refinement. The wtRBD-hACE2 (PDB ID: 6M0J) structures were manually docked into the refined maps of $RBD_{MASCp36}$-Fab_{B8}-Fab_{D14}-mACE2 complex using UCSF Chimera (*46*) and further corrected manually by real-space refinement in COOT (*47*). The atomic models were further refined by positional and B-factor refinement in real space using Phenix (*48*). Validation of the final model was performed with Molprobity (49). The data sets and refinement

bioRxiv preprint doi: https://doi.org/10.1101/2020.11.10.377333; this version posted November 11, 2020. The copyright holder for this preprint (which was not certified by peer review) is the author/funder, who has granted bioRxiv a license to display the preprint in perpetuity. It is made available under aCC-BY-NC-ND 4.0 International license.

statistics are shown in table S1.

Statistical analysis. Statistical analyses were carried out using Prism software (GraphPad). All data are presented as means ± standard error of the means (SEM). Statistical significance among different groups was calculated using the Student's *t* test, Fisher's Exact test, Two-way ANOVA or Mann-Whitney test *, **, and *** indicate $P < 0.05$, $P < 0.01$, and $P < 0.001$, respectively.

Reference and note:

42. A. Kucukelbir, F. J. Sigworth, H. D. Tagare, Quantifying the local resolution of cryo-EM density maps. *Nature methods* **11**, 63-65 (2014); published online EpubJan (10.1038/nmeth.2727).
43. E. F. Pettersen, T. D. Goddard, C. C. Huang, G. S. Couch, D. M. Greenblatt, E. C. Meng, T. E. Ferrin, UCSF Chimera--a visualization system for exploratory research and analysis. *Journal of computational chemistry* **25**, 1605-1612 (2004); published online EpubOct (10.1002/jcc.20084).
44. A. Brown, F. Long, R. A. Nicholls, J. Toots, P. Emsley, G. Murshudov, Tools for macromolecular model building and refinement into electron cryo-microscopy reconstructions. *Acta crystallographica. Section D, Biological crystallography* **71**, 136-153 (2015); published online EpubJan 1 (10.1107/s1399004714021683).
45. P. V. Afonine, R. W. Grosse-Kunstleve, N. Echols, J. J. Headd, N. W. Moriarty, M. Mustyakimov, T. C. Terwilliger, A. Urzhumtsev, P. H. Zwart, P. D. Adams, Towards automated crystallographic structure refinement with phenix.refine. *Acta crystallographica. Section D, Biological crystallography* **68**, 352-367 (2012); published online EpubApr (10.1107/s0907444912001308).
46. V. B. Chen, W. B. Arendall, 3rd, J. J. Headd, D. A. Keedy, R. M. Immormino, G. J. Kapral, L. W. Murray, J. S. Richardson, D. C. Richardson, MolProbity: all-atom structure validation for macromolecular crystallography. *Acta crystallographica. Section D, Biological crystallography* **66**, 12-21 (2010); published online EpubJan (10.1107/s0907444909042073).
47. S. H. Scheres, RELION: implementation of a Bayesian approach to cryo-EM structure determination. *Journal of structural biology* **180**, 519-530 (2012); published online EpubDec (10.1016/j.jsb.2012.09.006).
48. D. N. Mastronarde, Automated electron microscope tomography using robust prediction of specimen movements. *Journal of structural biology* **152**, 36-51 (2005); published online EpubOct (10.1016/j.jsb.2005.07.007).
49. N. van Doremalen, T. Lambe, ChAdOx1 nCoV-19 vaccine prevents SARS-CoV-2 pneumonia in rhesus macaques. **586**, 578-582 (2020); published online EpubOct (10.1038/s41586-020-2608-

bioRxiv preprint doi: https://doi.org/10.1101/2020.11.10.377333; this version posted November 11, 2020. The copyright holder for this preprint (which was not certified by peer review) is the author/funder, who has granted bioRxiv a license to display the preprint in perpetuity. It is made available under aCC-BY-NC-ND 4.0 International license.

Fig. S1.

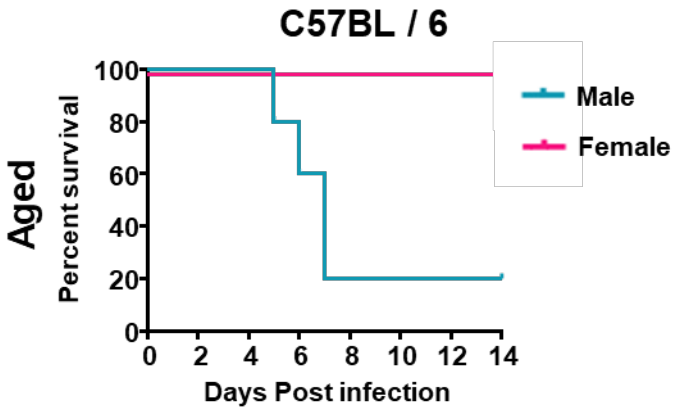

Fig. S1. Mortality of MASCp36 in C57BL/6 mice. Survival curve of female and male aged C57BL/6 mice (9-month-old) infected with 12,000 PFU of MASCp36 (n=6 per group).

.

bioRxiv preprint doi: https://doi.org/10.1101/2020.11.10.377333; this version posted November 11, 2020. The copyright holder for this preprint (which was not certified by peer review) is the author/funder, who has granted bioRxiv a license to display the preprint in perpetuity. It is made available under aCC-BY-NC-ND 4.0 International license.

Fig. S2.

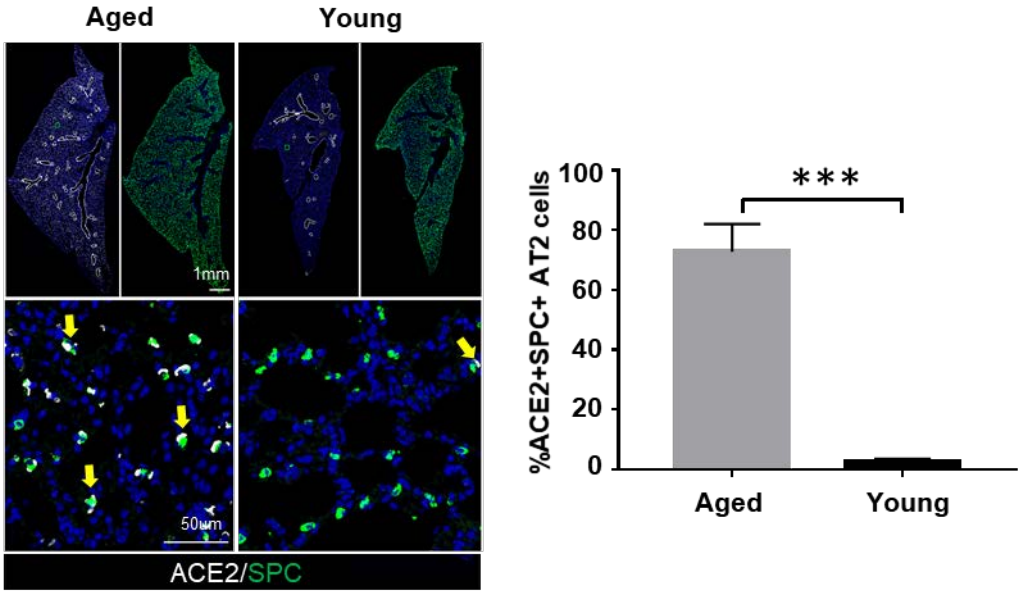

Fig. S2. ACE2 expression discrepancy in lungs of non-infected control aged and young mice. Multiplex immunofluorescence staining for detection of ACE2 (white) and SPC (green) expression in lung tissues from non-infected control aged and young mice. The framed areas are shown below at a higher magnification. The yellow arrows indicate $SPC^{+}ACE2^{+}$-double positive cells. The percentage of $ACE2^{+}SPC^{+}$-double positive cells in the SPC^{+} AT2 compartment was statistically analyzed. Data are presented as mean ± SD (n = 3).

bioRxiv preprint doi: https://doi.org/10.1101/2020.11.10.377333; this version posted November 11, 2020. The copyright holder for this preprint (which was not certified by peer review) is the author/funder, who has granted bioRxiv a license to display the preprint in perpetuity. It is made available under aCC-BY-NC-ND 4.0 International license.

Fig. S3.

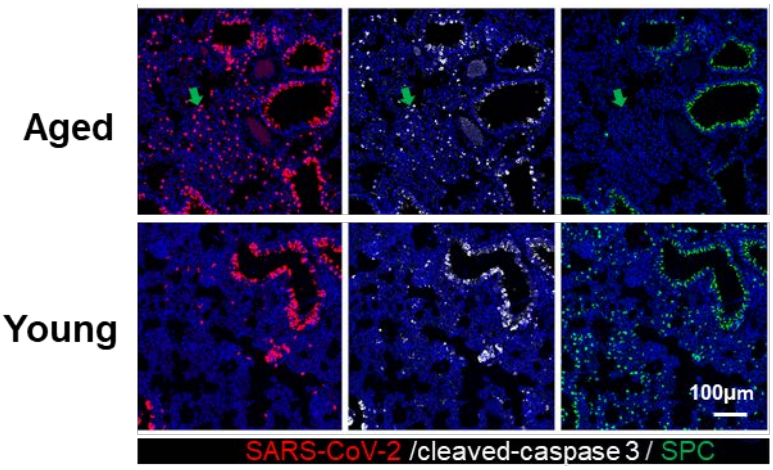

Fig. S3. MASCp36 cellular tropism causes differential apoptosis in lungs from young and aged mice. Multiplex immunofluorescence staining for detection of SARS-CoV-2 N protein (red), cleaved-caspase 3 (white) and SPC (green) expression in lung tissues of aged and young mice at 1 dpi. The green arrows indicate apoptotic cells with MASCp36 infection in the alveolar region.

bioRxiv preprint doi: https://doi.org/10.1101/2020.11.10.377333; this version posted November 11, 2020. The copyright holder for this preprint (which was not certified by peer review) is the author/funder, who has granted bioRxiv a license to display the preprint in perpetuity. It is made available under aCC-BY-NC-ND 4.0 International license.

Fig. S4.

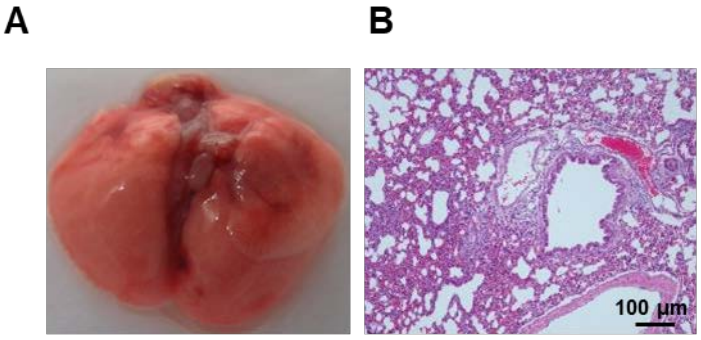

Fig. S4. Lung damage of young BALB/c mice infected with MASCp36. Young BALB/c mice were i.n. inoculated with 12,000 PFU of MASCp36, and sacrificed at 4 dpi. (A) Gross appearance of mouse lung and (B) Hematoxylin and eosin (H&E) staining of lung sections.

bioRxiv preprint doi: https://doi.org/10.1101/2020.11.10.377333; this version posted November 11, 2020. The copyright holder for this preprint (which was not certified by peer review) is the author/funder, who has granted bioRxiv a license to display the preprint in perpetuity. It is made available under aCC-BY-NC-ND 4.0 International license.

Fig. S5.

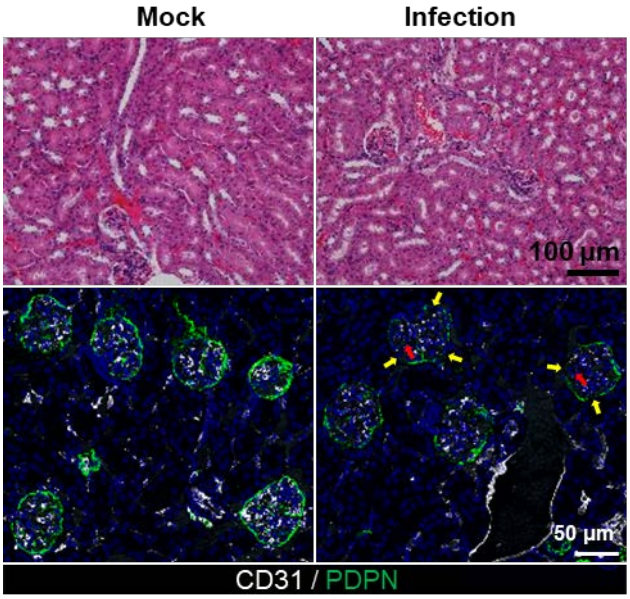

Fig. S5. Glomerular injury in BALB/c mice with MASCp36 infection. Hematoxylin and eosin (H&E) staining of kidney sections from aged BALB/c mice infected with MASCp36 at 4 dpi (n=3 per group). Multiplex immunofluorescence staining of mouse kidney sections for CD31(white) and PDPN (green). The yellow and red arrows indicate discrete glomerular basement membrane and endothelial vessels, respectively.

bioRxiv preprint doi: https://doi.org/10.1101/2020.11.10.377333; this version posted November 11, 2020. The copyright holder for this preprint (which was not certified by peer review) is the author/funder, who has granted bioRxiv a license to display the preprint in perpetuity. It is made available under aCC-BY-NC-ND 4.0 International license.

Fig S6

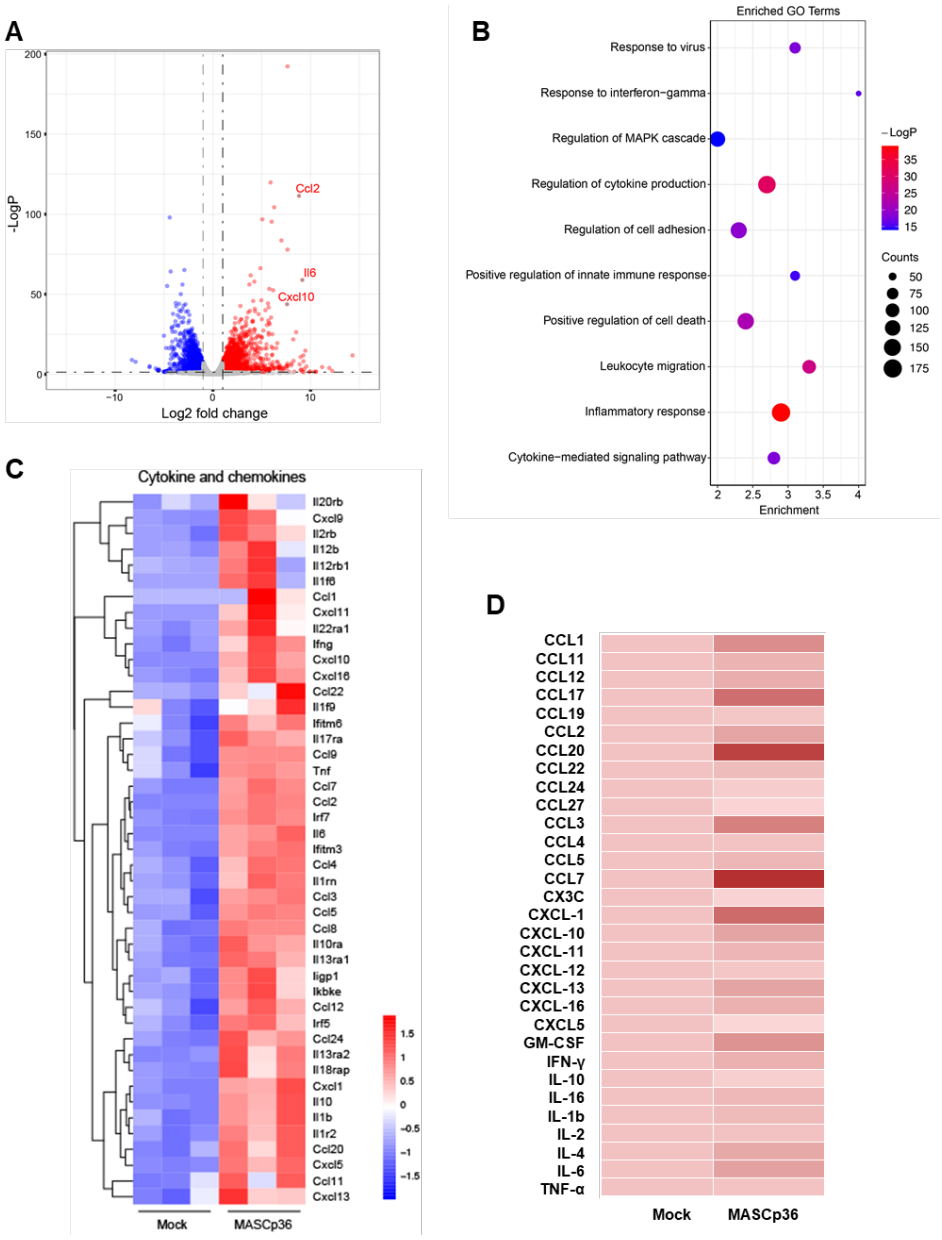

Fig S6. Pulmonary inflammatory response in mice infected with MASCp36. Male aged BALB/c mice were i.n. inoculated with 12,000 PFU of MASCp36, and sacrificed at 4 dpi. (A) Volcano plots indicating differential regulated genes after MASCp36 infection. Up-regulated genes (padj < 0.05) with a log2 (fold change) of more than 1 are indicated in red, down-regulated genes (padj < 0.05) with a log2 (fold change) of less than -1 are indicated in blue. (B) Dot plot visualization of enriched GO terms of up-regulated genes. Gene enrichment analyses were performed using Metascape against the GO dataset for biological processes. The color of the dots represents the –LogP value for each enriched GO term, and size represents the number of genes enriched in each GO term. (C)

bioRxiv preprint doi: https://doi.org/10.1101/2020.11.10.377333; this version posted November 11, 2020. The copyright holder for this preprint (which was not certified by peer review) is the author/funder, who has granted bioRxiv a license to display the preprint in perpetuity. It is made available under aCC-BY-NC-ND 4.0 International license.

Heatmap indicating the expression patterns of 45 cytokine and chemokine genes. Colored bar represents Z-score of log2 transformed TPM+1. (D) Cytokine and chemokine analysis was done by Luminex.

bioRxiv preprint doi: https://doi.org/10.1101/2020.11.10.377333; this version posted November 11, 2020. The copyright holder for this preprint (which was not certified by peer review) is the author/funder, who has granted bioRxiv a license to display the preprint in perpetuity. It is made available under aCC-BY-NC-ND 4.0 International license.

Fig S7

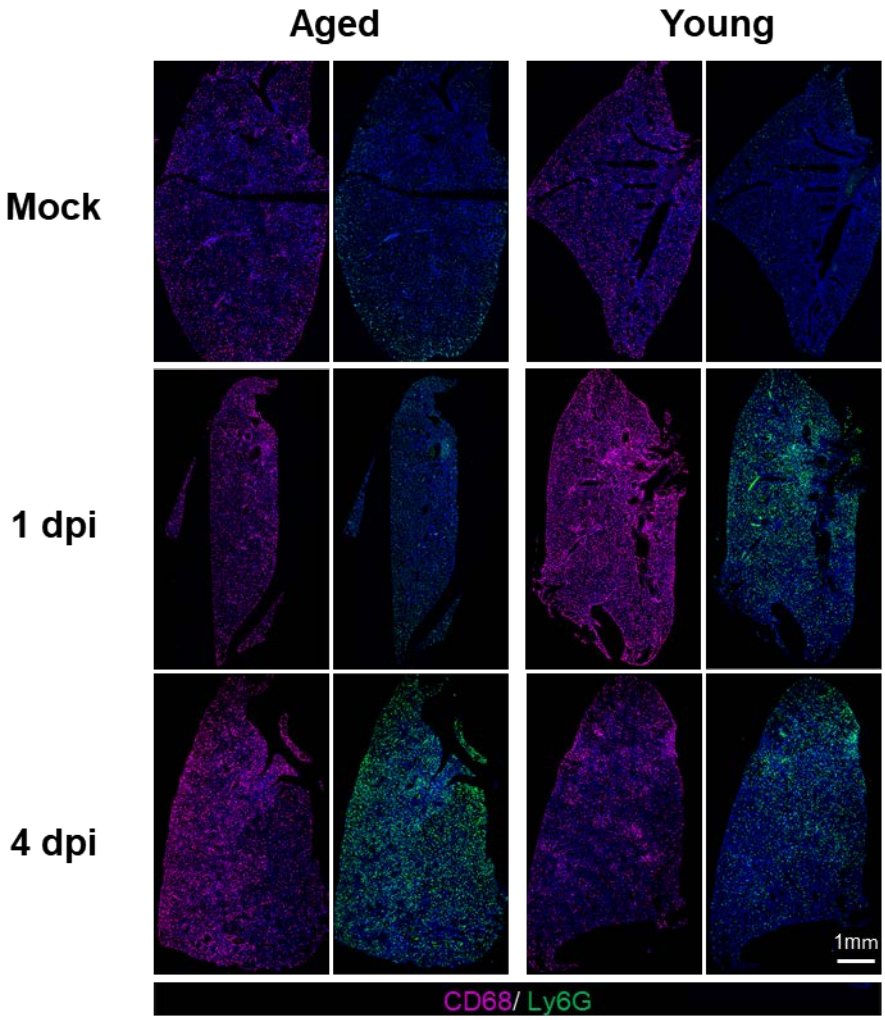

Fig. S7. Infiltration of macrophages and neutrophils in lungs of BALB/c mice during MASCp36 infection. Multiplex immunofluorescence staining of mouse lung sections for detection of $CD68^+$ macrophages (magenta) and Ly-$6G^+$ neutrophils (green) at 1 dpi and 4 dpi.

bioRxiv preprint doi: https://doi.org/10.1101/2020.11.10.377333; this version posted November 11, 2020. The copyright holder for this preprint (which was not certified by peer review) is the author/funder, who has granted bioRxiv a license to display the preprint in perpetuity. It is made available under aCC-BY-NC-ND 4.0 International license.

Fig S8

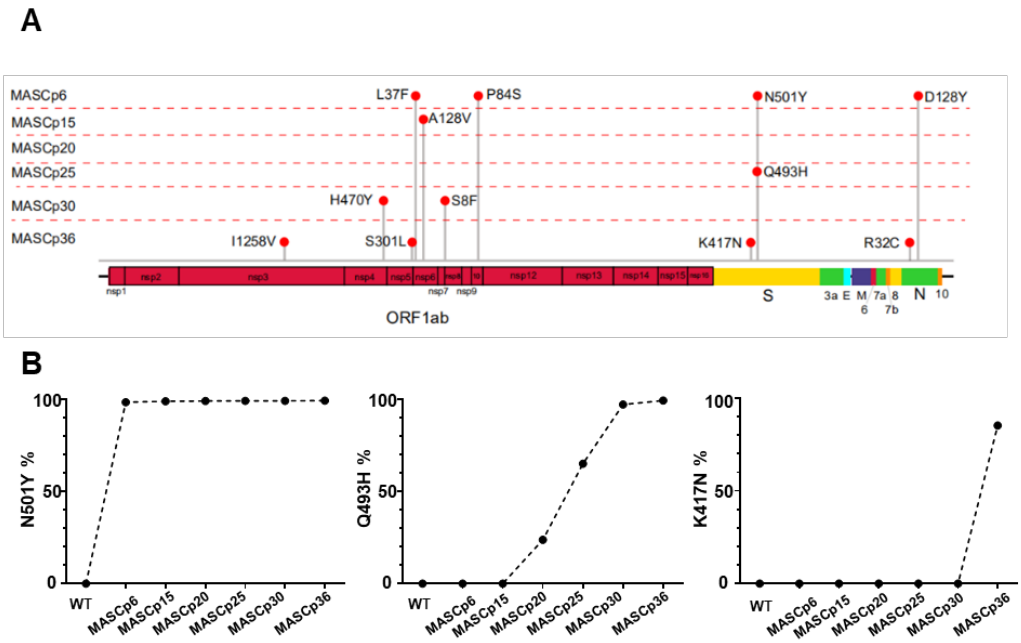

Fig S8. Adaptive mutations identified in different mouse adapted strains. (A) Schematic diagram of SARS-CoV-2 genome and all the adaptive mutations. (B) The proportion of N501Y, Q493H, K417N mutations located on the RBD.

bioRxiv preprint doi: https://doi.org/10.1101/2020.11.10.377333; this version posted November 11, 2020. The copyright holder for this preprint (which was not certified by peer review) is the author/funder, who has granted bioRxiv a license to display the preprint in perpetuity. It is made available under aCC-BY-NC-ND 4.0 International license.

Fig S9

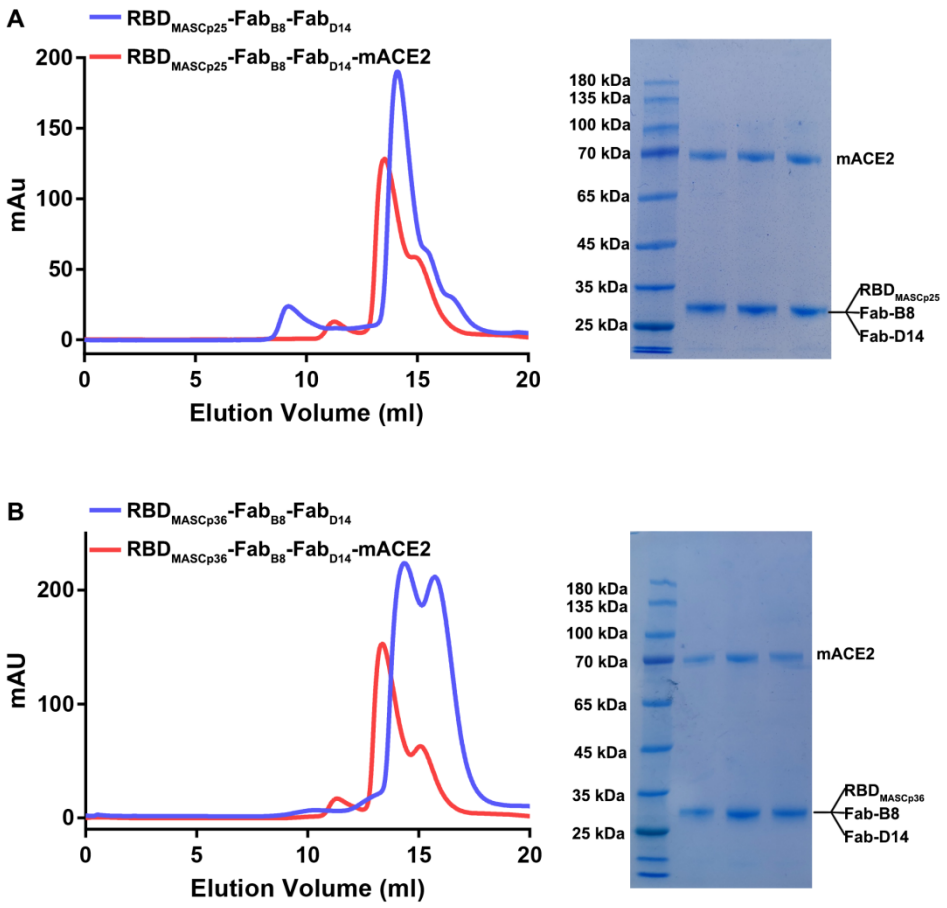

Fig S9. Purification and characterization of $RBD_{MASCp25}$-Fab_{B8}-Fab_{D14}-mACE2 complex and $RBD_{MASCp36}$-Fab_{B8}-Fab_{D14}-mACE2 complex. (A) Gel filtration profiles of the ternary complex ($RBD_{MASCp25}$-Fab_{B8}-Fab_{D14}, colored by blue line) and quaternary complex ($RBD_{MASCp25}$-Fab_{B8}-Fab_{D14}-mACE2, colored by red line). (B) SDS-PAGE analysis of the $RBD_{MASCp25}$-Fab_{B8}-Fab_{D14}-mACE2 complex. (C) Gel filtration profiles of the ternary complex ($RBD_{MASCp36}$-Fab_{B8}-Fab_{D14}, colored by bule line) and quaternary complex ($RBD_{MASCp36}$-Fab_{B8}-Fab_{D14}-mACE2, colored by red line). (D) SDS-PAGE analysis of the $RBD_{MASCp36}$-Fab_{B8}-Fab_{D14}-mACE2 complex.

bioRxiv preprint doi: https://doi.org/10.1101/2020.11.10.377333; this version posted November 11, 2020. The copyright holder for this preprint (which was not certified by peer review) is the author/funder, who has granted bioRxiv a license to display the preprint in perpetuity. It is made available under aCC-BY-NC-ND 4.0 International license.

Fig S10

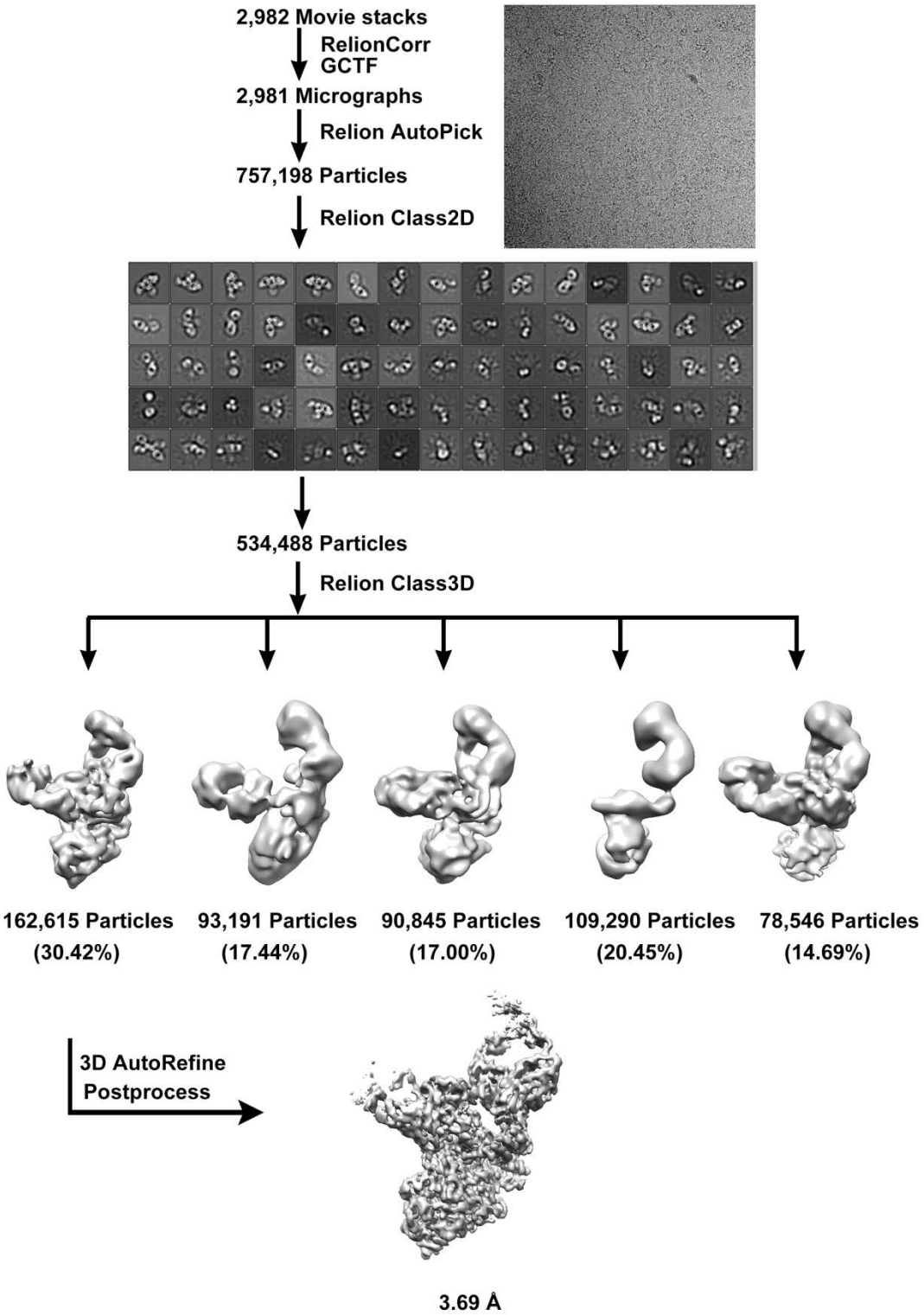

Fig S10. Flow chart for the Cryo-EM data processing of $RBD_{MASCp36}$-Fab_{B8}-Fab_{D14}-mACE2 complex.

bioRxiv preprint doi: https://doi.org/10.1101/2020.11.10.377333; this version posted November 11, 2020. The copyright holder for this preprint (which was not certified by peer review) is the author/funder, who has granted bioRxiv a license to display the preprint in perpetuity. It is made available under aCC-BY-NC-ND 4.0 International license.

Fig S11

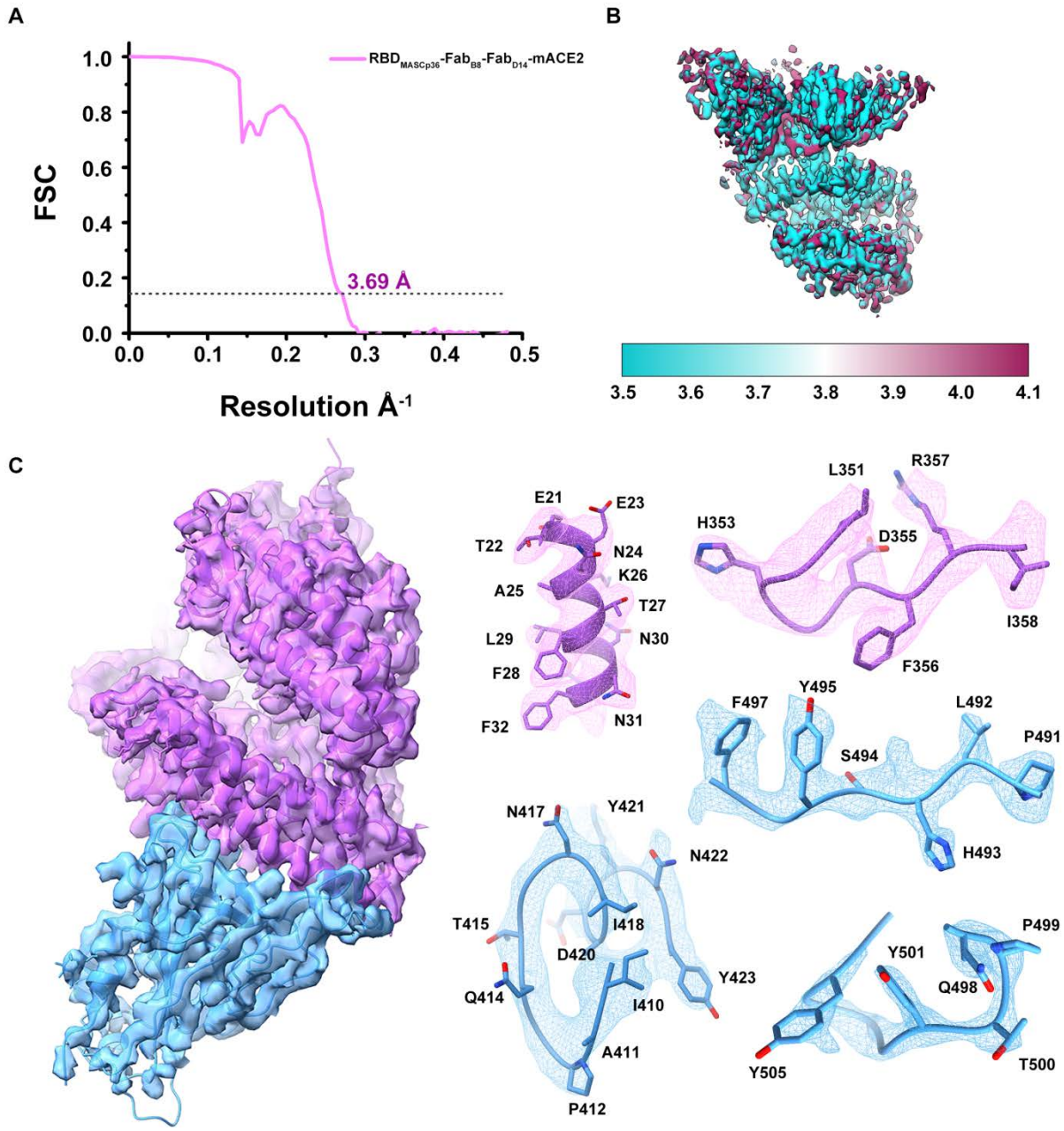

Fig S11. Cryo-EM images and resolution evaluation of the EM map of $RBD_{MASCp36}$-Fab_{B8}-Fab_{D14}-mACE2 complex. (A) The gold-standard FSC curve of the final map. (B) Local resolution assessments of cryo-EM maps. Local-resolution evaluation of the map of the $RBD_{MASCp36}$-Fab_{B8}-Fab_{D14}-mACE2 complex using ResMap (*35*) is shown. (C-D) Electron density maps at the interface between the $RBD_{MASCp36}$ (colored in cyan) and mACE2 (colored in purple).

bioRxiv preprint doi: https://doi.org/10.1101/2020.11.10.377333; this version posted November 11, 2020. The copyright holder for this preprint (which was not certified by peer review) is the author/funder, who has granted bioRxiv a license to display the preprint in perpetuity. It is made available under aCC-BY-NC-ND 4.0 International license.

Fig S12.

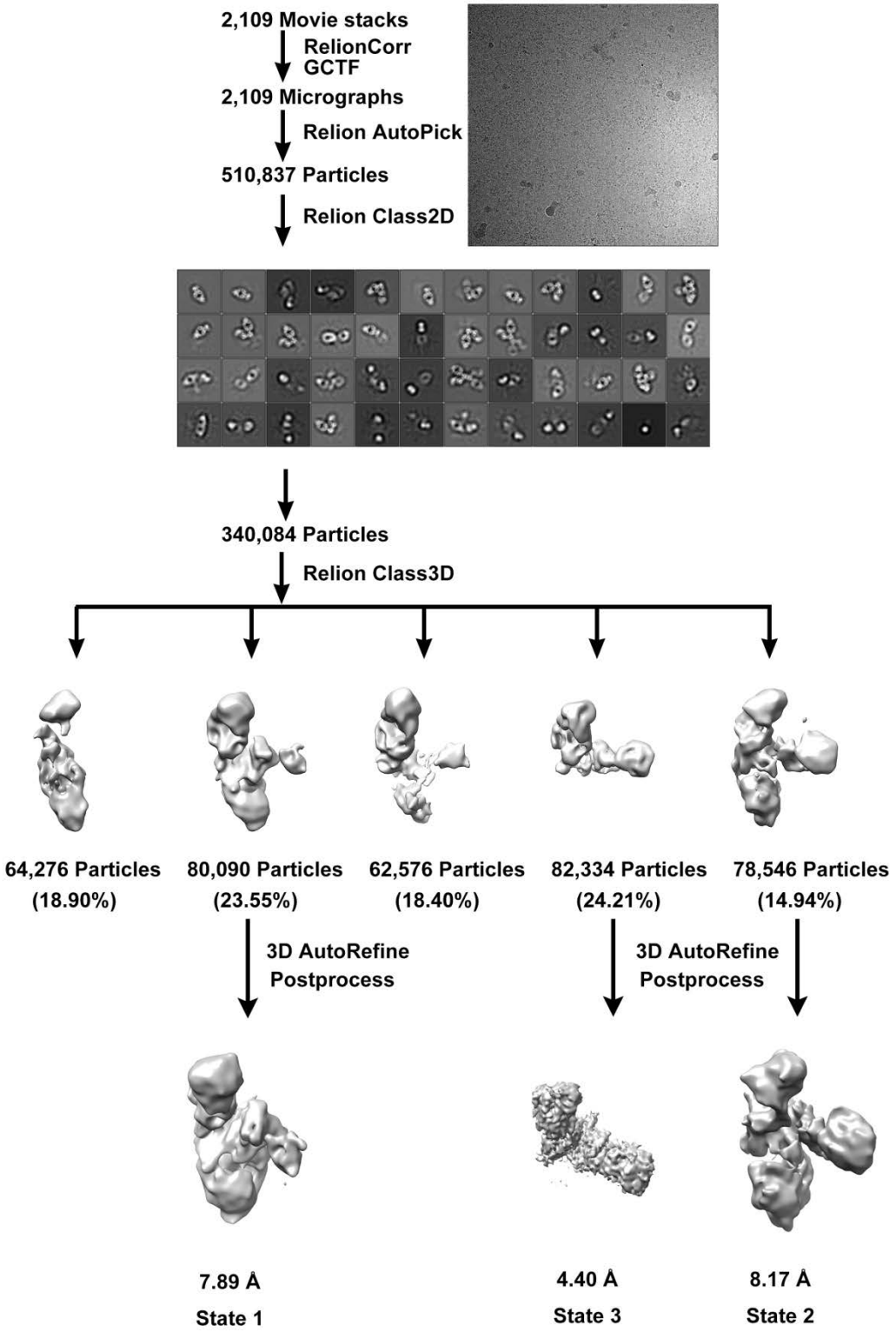

Fig S12. Flow chart for Cryo-EM data processing of $RBD_{MASCp25}$-Fab_{B8}-Fab_{D14}-mACE2 complex.

bioRxiv preprint doi: https://doi.org/10.1101/2020.11.10.377333; this version posted November 11, 2020. The copyright holder for this preprint (which was not certified by peer review) is the author/funder, who has granted bioRxiv a license to display the preprint in perpetuity. It is made available under aCC-BY-NC-ND 4.0 International license.

Fig S13

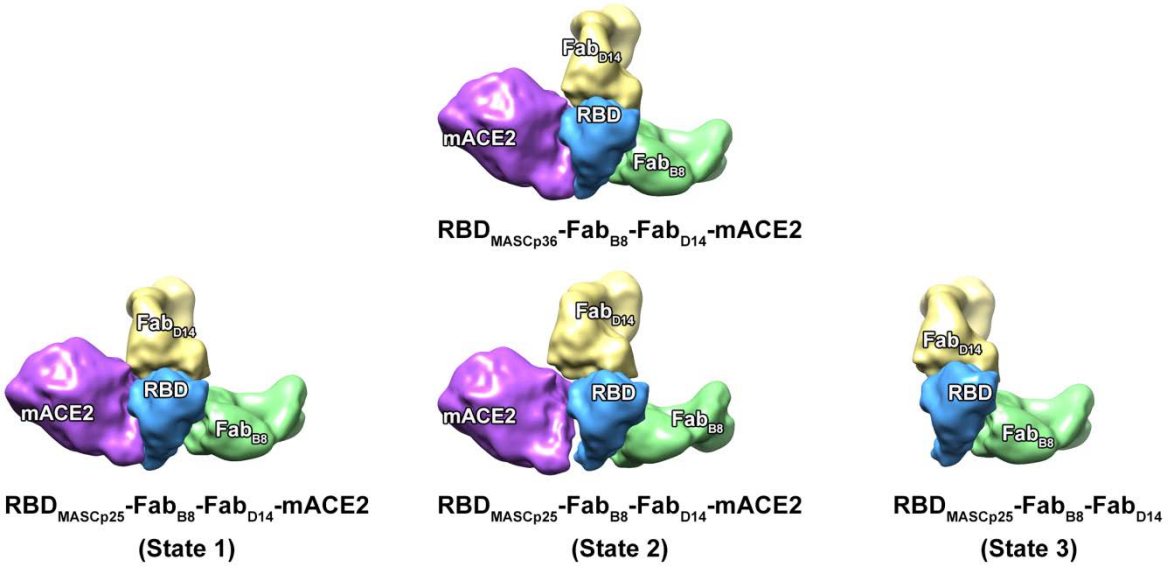

Fig S13. Comparison of RBD$_{MASCp36}$-Fab$_{B8}$-Fab$_{D14}$-mACE2 complex with different conformations of RBD$_{MASCp25}$-Fab$_{B8}$-Fab$_{D14}$-mACE2 complex. All the subunits were filtered to a lower resolution at 15 Å. RBD mutant, mACE2, Fab$_{B8}$ and Fab$_{D14}$ are colored in blue, purple, yellow and green, respectively.

bioRxiv preprint doi: https://doi.org/10.1101/2020.11.10.377333; this version posted November 11, 2020. The copyright holder for this preprint (which was not certified by peer review) is the author/funder, who has granted bioRxiv a license to display the preprint in perpetuity. It is made available under aCC-BY-NC-ND 4.0 International license.

Table S1 Cryo-EM data collection and atomic model refinement statistics

Data collection and reconstruction statistics	
Protein	$RBD_{MASCp36}$-Fab_{B8}-Fab_{D14}-mACE2
Voltage (kV)	300
Detector	K2
Pixel size (Å)	1.04
Electron dose (e^-/Å^2)	60
Defocus range (μm)	1.25-2.7
Final particles	162,615
Final resolution (Å)	3.69
Models refinement and validation statistics	
Ramachandran statistics	
Favored (%)	92.38
Allowed (%)	7.43
Outliers (%)	0.11
Rotamer outliers (%)	0.09
R.m.s.d	
Bond lengths (Å)	0.02
Bond angles (°)	1.26

bioRxiv preprint doi: https://doi.org/10.1101/2020.11.10.377333; this version posted November 11, 2020. The copyright holder for this preprint (which was not certified by peer review) is the author/funder, who has granted bioRxiv a license to display the preprint in perpetuity. It is made available under aCC-BY-NC-ND 4.0 International license.

Table S2. Residues of $RBD_{MASCp36}$ interacting with mACE2 at the binding Interface (d < 4 Å)

$RBD_{MASCp36}$ Residues	mACE2
N417	N30
	Q34
L455	Q34
F456	N31
A475	T27
F486	S82
N487	N24
Y489	T27
	F28
	N31
H493	N31
	E35
G496	D38
Q498	Q42
	L45
T500	Y41
	L45
	D355
	K357
Y501	Y41
	H353
	G354
G502	H353
	G354
Y505	H353